NTNU

Norwegian University of
Science and Technology

Patterning of Hard Mask on (111)-Oriented BTO/LSMO Heterostructures on STO Substrates

Einar Standal Digernes

Nanotechnology
Submission date: July 2016
Supervisor: Thomas Tybell, IET

Norwegian University of Science and Technology
Department of Electronics and Telecommunications

ABSTRACT

Functional oxides exhibit properties that make them interesting for future electronic devices. Thin films of functional oxides can be routinely produced, but there lacks a standard technique for establishing nanoscale freestanding structures on insulating substrates. The nanostructures must be well defined and maintain bulk properties.

In this work a recipe for establishing a two layer hard mask suitable for ion beam etching (IBE) has been developed. A chromium hard mask is patterned and deposited using electron beam lithography (EBL) and lift off. The pattern is transferred to an underlying carbon layer by oxygen reactive ion etching (RIE).

Hard masks with hallbar patterns have been structured on 5×5 mm samples with thin films of $La_{0.7}Sr_{0.3}MnO_3$ (LSMO) and $BaTiO_3$ (BTO) on (111)-oriented $SrTiO_3$ (STO) substrates. The hallbars have widths from 11 µm and down to 130 nm, which are connected to 200×200 µm contacts pads.

A bilayer mask of PMMA and MMA with a total thickness of 240 nm is found to work successfully for lifting off 20 nm of chromium. Samples are prone to charging during electron beam lithography. Fine features are written using 100 pA beam current, while large features are defined at 10 nA.

The hard mask patterned samples are prepared for IBE, which will transfer the hard mask pattern into the oxide thin film and substrate, realizing freestanding oxide structures. Followed by deposition of contacts and wirebonding, the devices can be used to investigate electrical transport properties.

SAMANDRAG

Funksjonelle oksid viser eigenskapar som gjer dei interessante for framtidige elektroniske komponentar. Tynnfilmar av funksjonelle oksid kan bli rutinemessig produsert, men det manglar ei standard metode for å etablere nanoskala frittståande strukturar på isolerande underlag. Nanostrukturane må ha godt definerte geometriar der bulkeigenskapane er tatt i vare.

I dette arbeidet er ei oppskrift for å etablere frittståande strukturar på isolerande underlag blitt utvikla. Ei krom-maske er mønstra og deponert ved hjelp av elektronstrålelitografi (ESL) og elektronstråledamping. Mønsteret overførast til eit underliggande lag av karbon med oksygen reaktiv-ioneesting (RIE).

Masker med Hallbar-mønster er strukturert på 5×5 mm-prøver med tynnfilmar av $La_{0.7}Sr_{0.3}MnO_3$ (LSMO) og $BaTiO_3$ (BTO) på (111)-orientert $SrTiO_3$ (STO) underlag. Hallbarane har breidder frå 11 µm og ned til 130 nm, og er kople til 200×200 µm kontaktflater.

Ei to-lagsmaske av PMMA og MMA med ein total tjukkleik på 240 nm er funnen brukbar for å lyfte av 20 nm med krom. Prøvene er utsette for opplading under ESL. For å oppretthalde høg skrivehastigheit blir store strukturar definerte med ein straum på 10 nA, medan små strukturar blir skrivne med ein straum på 100 pA.

Prøver er førebudd med masker slik dei i framtida kan mønstrast med ionestråleetsing. Det vil overføre mønsteret frå maska til tynnfilmane og underlaget slik at frittståande strukturar blir oppretta. Vidare vil kontakter deponerast og ledningar bindast, slik at komponentane kan brukast til å undersøke elektroniske transporteigenskapar.

PREFACE

This thesis is written in the Spring of 2016 at the Department of Electronics and Telecommunication at the Norwegian University of Science and Technology as fulfillment of the requirement for the degree as Master of Science in Nanotechnology.

Recently, a method for growth of epitaxial films of (111)-oriented perovskite oxides has been established in the oxide electronics group at NTNU. Heterostructures of BTO and LSMO can be grown using this method, and are expected to exhibit altered properties, as well as strain mediated coupling at the interface. In this work a method for establishing nanoscale freestanding structures from perovskite oxide thin films is developed.

The method is inspired by a technique developed by Åsmund Monsen, but has been adapted to the equipment in the NTNU NanoLab cleanroom. Several technical issues were encountered throughout the semester, the most critical being the IBE going down in the middle of April, and not coming back up again. Because of the technical issues, the work has been on the process leading up to the etching step. Much time has been spent on becoming proficient on the new Elionix G-100 EBL. While the original objective of the work was not accomplished, the results from this work will be valuable for future users who wish to establish nanostructures from functional oxide thin films.

Five samples with BTO and LSMO thin films have been prepared with hard masks featuring hallbar geometries. As soon as the IBE is back in service, these samples can be prepared with only a few process steps for performing transport measurements.

I would like to extend my gratitude to my supervisor *Thomas Tybell* for guiding me through the work and providing valuable feedback. I would also like to thank my coadvisor *Torstein Bolstad* for making the sample structures and discussing my work. I thank *Kristoffer Kjærnes* for the fruitful discussion and inspiring conversations while working in the cleanroom. I would also like to thank the staff at the NTNU NanoLab for providing support throughout the project. The Research Council of Norway is acknowledged for the support to NTNU NanoLab through the Norwegian Micro- and Nano-Fabrication Facility, NorFab (197411/V30).

Finally, I thank my friends and family for their support during my memorable years at NTNU.

July 3, 2016
Houston, Texas, USA

Einar Standal Digernes

CONTENTS

LIST OF FIGURES

LIST OF TABLES

Chapter 1

INTRODUCTION

In this first chapter an introduction to the work is given. First, background information is covered to motivate why the material system in this work is interesting. Then, a brief overview of state-of-the-art nanofabrication of functional oxides is given. The last part of this chapter presents the project outline.

1.1 Motivation

Magnetism is an intriguing group of physical phenomenas that originate from magnets. The first documented observation of permanent magnetism, ferromagnetism, was made in the naturally occurring mineral magnetite Fe_3O_4 almost three thousand years ago[1]. The technological impact has been tremendous, with applications ranging from the first primitive compasses, electromagnetic motors and to advanced magnetic storage devices used today.

Our understanding of magnetism has evolved the last hundred of years, and we now know that the magnetic properties of materials originate from the collective response of electronic spins in conjunction with their orbital motion. In some materials the interaction between neighboring spins, quantified by the exchange term, gives rise to ferromagnetic or anti-ferromagnetic ordering.

The discovery of how the electron spin degree of freedom can be used to carry information in electronic circuits has given birth to the field of spin-electronics, or spintronics[2–5]. The observation of the giant magnetoresistive effect (GMR) in 1988 was of such scientific impact that the two discoverers were awarded the Nobel Prize in physics in 2007[6, 7]. The GMR is observed as a significant change in electrical resistance if the magnetizations of two adjacent ferromagnetic layers, separated by a thin non-magnetic layer, are parallel or antiparallel. Later, several other spin dependent electron transport effects have been observed. One of these is the tunneling magnetoresistance (TMR) utilized in the magnetic tunnel junction (MTJ). MTJs are used in the read-heads of modern hard disk drives and in non-volatile magnetic random access memory (MRAM).

Following the predictions of Moore's law the number of transistors on a device has increased exponentially the last fifty years[8]. The industry has achieved this through downscaling of the transistor. The increase in performance has been followed by an increased demand for computer storage, and a similar scaling rule has applied to increase the areal density for storage of data bits[9].

The focus on miniaturization has brought electronics into the field of nanotechnology. With critical dimensions approaching only a few nanometer in size the quantum mechanical nature of the electron has to be considered. Leakage by electron tunneling through thin barriers makes devices less power efficient and results in heating issues. At the smallest scales magnetic memory devices face the superparamagnetic limit[10], where thermal energy causes the magnetic state to flip unintendedly. Down scaling is also an economical issue since moving down in size requires the building of brand new fabrication lines costing multiple billions of dollars. Hence, due to the issues with further downscaling the industry has called for the end of Moore's law [11].

The industry is now shifting its research and development focus. The concept of More than Moore was born in 2010 and is the idea of improving device performance through new functionalities [12]. An example is the substitution of energy intensive magnetic field writing of MRAM with spin transfer torque [13, 14].

A more ambitious approach is to replace the materials used in spintronic devices today with materials from the novel field of oxide based electronics [15–17]. Strongly correlated electron effects in oxide materials give a rich variety of electronic phases, such as ferromagnetism, ferroelectricity, multiferrocity, high-κ dielectricity, colossal magnetoresistivity (CMR), spin polarization and high temperature superconductivity[18–25]. Combining these properties gives the opportunity to create truly novel devices.

When Herbert Kroemer during his Nobel lecture stated "the interface is the device" [26] he was primarily aiming at the field of semiconductors. This also holds true for oxide devices. When two oxide materials are brought together, the strongly correlated electron nature can result in electronic reconstruction at the interface and the occurrence of extraordinary electron systems. Two-dimensional electron gases [27] and superconductivity [28] have been observed at the interface between two insulating oxides. To enable spintronic devices from oxide materials require fundamental knowledge of what happens at the interface. That way the electronic properties can be tailored to meet the needs in future components.

An effect of special interest for new magnetic memory devices is the magnetoelectric (ME) coupling. The ME coupling enables control of magnetism with electric fields, and vice versa. Realization of strong ME coupling will open up for a new class of magnetic memory where the states are switched using electric fields, thereby greatly reducing the energy consumption compared to current devices [29, 30].

One of the great challenges today is to find a material with a strong ME coupling at room temperature. A promising approach is to use oxide thin film heterostructures, where the ME coupling occurs at the interface between a ferroelectric and a ferromagnetic layer.

Recently, growth of high quality thin films in the (111)-direction has been accomplished [31, 32]. The symmetry at the interface is altered when the

orientation is changed from (100) to (111), and this might result in a stronger ME coupling.

A potential candidate for stronger ME coupling is the thin film heterostructure of ferroelectric $BaTiO_3$ and ferromagnetic $La_{0.7}Sr_{0.3}MnO_3$ (LSMO) grown on top of (111)-oriented $SrTiO_3$ (STO). Signs of ME coupling have already been observed at the interface of (100)-oriented BTO/LSMO as discontinuous jumps in the resistivity [33].

1.2 State-of-the-art

Advances in nanofabrication technology have enabled downscaling of perovskite based microelectronics into the nanoscale dimension. At the nanoscale, dramatic changes in the electrical and transport properties of manganite nanostructures have been observed, such as ultrasharp jumps of magnetoresistance, reentrant metal insulator transition, negative differential resistances, and intrinsic tunneling magnetoresistance[34–40]. In the past couple of years new synthetic fabrication methods for creating nanoscale structures have been developed to enable further studies of the effects at reduced dimensionality.

Sol-gel technique has been used to grow particles of $La_{0.25}Ca_{0.75}MnO_3$ with sizes ranging from 40 to 2000 nm[41]. Hydrothermal synthesis of $La_{0.5}Ba_{0.5}MnO_3$ nanowires several micrometers in length and typical widths of 30 to 130 nm has been achieved[42, 43]. Nanowires of $La_{0.67}Sr_{0.33}MnO_3$ with 80 nm diameter have been grown with electrospinning process[44]. With the template method $La_{0.67}Ca_{0.33}MnO_3$ nanowires with an average diameter of 65 nm have been grown[45]. Optical lithography combined with wet etching have been used to define micrometer sized devices from $(La_{1-y}Pr_y)_xCa_{1-x}MnO_3$[34, 36–38]. Bridges with dimensions down to 100 nm of (La,Pr,Ca)MnO_3 have been fabricated using a focused ion beam[40, 46]. Using a combination of electron beam lithography (EBL) and ion beam etching freestanding ellipses with short axis down to 150 nm have been defined from $La_{0.7}Sr_{0.3}MnO_3$ thin films on Nb:STO substrates[47], and 50 nm embedded patterns have been achieved using low energy ion beam irradiation[48].

However, there lacks a technique for establishing nanoscale freestanding structures from thin films on insulating substrates. Two commonly used dry etching techniques are reactive ion etching (RIE) and ion beam etching (IBE). RIE is handicapped on insulating substrates due to charging effects, which renders RIE unsuitable for establishing small structures. An IBE is equipped with an electron emitting element that neutralize the ion beam, thereby eliminating the requirement of a conductive sample.

1.3 Project Outline

This work is part of a project where the goal is to establish nanoscale freestanding structures from functional oxides on insulating substrates, maintaining bulk properties. The recipe is inspired by the technique used by Åsmund Monsen [47], and is based on establishing a chromium-carbon hard mask with EBL and etching with IBE. The recipe was adapted to the equipment at the NTNU NanoLab during my project work[49]. The functional oxides to be studied are heterostructures of LSMO and BTO on (111)-oriented STO.

The objective of my part of the project was to establish freestanding structures, and perform transport measurements on these to test if bulk properties are maintained. However, due to severe instrument down time, it was not possible to perform the final IBE etching step. Therefore, the focus on this work has been shifted to optimizing the process for establishing the chromium-carbon hard mask.

The hard mask used in this project consist of two layers. The top layer is chromium and is structured by EBL. The bottom layer is carbon, and is structured using oxygen reactive ion etching with the chromium layer as hard mask. The pattern of the final freestanding devices after IBE is directly related to the hard mask pattern, which is why optimizing the process for establishing the hard mask is of interest.

The hard mask is structured with a hallbar geometry. The hallbar geometry is chosen so the resistivity, carrier sign and carrier density can be determined. The effect of the nanostructuring process on the bulk properties can thus be investigated based on the change in the transport properties.

Following this introduction, chapter 2 covers theory on the properties of functional oxides, as well as hall theory. Chapter 3 presents the nanostructuring techniques used in this work, with focus on EBL, thin film deposition and nanoscale pattern transfer. Then, chapter 4 presents the experimental method, including process development and hard mask fabrication. Next, in chapter 5 the results from the process development and nanostructuring is presented and discussed. Directions for further work are given. Finally the conclusions from the work are summarized in chapter 6.

Chapter 2

THEORY

This chapter will cover the theory necessary to understand the magnetic and transport properties in perovskite manganites, and how they can be manipulated in heterostructures. The Hall effect, which can be used to characterize transport properties, is also introduced.

The content in this chapter was written with the objective of explaining the results from transport measurements on freestanding structures. However, because freestanding structures were not established due to technical issues, there is no measurement data to which this theory can be applied. The theory is included because it explains why the material system used in this project is interesting, as well as why Hall measurements are valuable.

2.1 Perovskite Crystal Structure

The materials used in this project have the perovskite crystal structure. The unit cell can be described chemically by ABO_3, where B is a small cation, and A is a cation about the size of the oxygen anion. The ideal unit cell can be described as cubic with the A-cation at the corners, B-cation in the center and the oxygen atoms forming an octahedron around the B-cation, as illustrated in figure 2.1. Depending on the relative sizes of the A and B cations and electronic structure, the unit cell can be distorted.

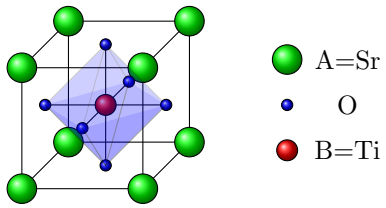

Figure 2.1: The cubic perovskite crystal structure with general chemical formula ABO_3, here examplified for $SrTiO_3$. The A cation is located at the corners, while the smaller B cation is located in the body center with the oxygen anions forming an octahedral cage around it.

Three materials with the perovskite crystal structure have been used in this project. Strontium titanate (STO) is one of them, and it has the chemical formula $SrTiO_3$ and cubic perovskite unit cell. STO is insulating and has a lattice

parameter of a = 3.905 Å, and is often used as a substrate for growth of other perovskite oxides[50]. STO can be made conductive through doping with low concentrations of niobium, typically 0.05 wt%.

The other two materials are lanthanum strontium manganite (LSMO) and barium titanate (BTO).

2.2 Perovskite Oxide Manganites

Perovskite oxide manganites, or simply manganites, is a group of strongly correlated electron (SCE) materials that have received much attention due to their unusual electron-transport and magnetic properties. The general chemical formula is $RE_{1-x}AE_xMnO_3$, where RE is a trivalent rare-earth and AE is a divalent alkaline-earth element. Manganites can exhibit the colossal magnetoresistance (CMR) effect[51–54], which can give a change in resistivity by several orders of magnitude, as a function of temperature, electric field, magnetic field and more[55–57]. The same transition is accompanied by a change from paramagnetic to ferromagnetic ordering as temperature is lowered.

The effect of doping x has a direct effect on the oxidation state of the manganese ion. Through doping a RE^{3+} is substituted by AE^{2+}, and is balanced by the oxidation state of Mn^{3+} changing to Mn^{4+}. For the case of $La_{1-x}Sr_xMnO_3$ the effect of doping has been studied at various doping levels[53, 58, 59]. At strontium concentrations $0 \leq x \leq 0.1$ the material is a Mott insulator and A-type antiferromagnet. Between $0.2 \leq x \leq 0.4$ LSMO is conducting and ferromagnetic, while in the range $0.5 \leq x \leq 0.75$ insulating and CE-type antiferromagnetic with charge ordering. For $0.75 \leq x \leq 0.85$ it magnetic order changes to C-type antiferromagnetic, and at $0.9 \leq x \leq 1.0$ it is G-type antiferromagnetic.

2.2.1 Electronic states in LSMO

The first step in understanding the transport properties of LSMO is to look at the electronic states of the manganese ion. In SCE materials the one-particle model breaks down, and the electrons cannot be treated as independent particles moving through a crystal barely interacting with each other. Electron-electron interactions must be taken into account. Following is an explanation of how crystal field splitting and Jahn Teller distortions affect the electronic states and band filling in LSMO.

Crystal field splitting describes the breaking of degeneracy when orbitals of neighboring atoms overlap, such as for the five degenerate d-orbitals of Mn with the p-orbital of oxygen in LSMO. When placed in an oxygen octahedral, the d-orbitals pointing in the x, y and z direction ($d_{x^2-y^2}$ and $d_{3z^2-r^2}$, called e_g) will have

a higher energy than the orbitals pointing between the oxygen ions (d_{xy}, d_{yz} and d_{zx}, called t_{2g}), as illustrated in figure 2.2.

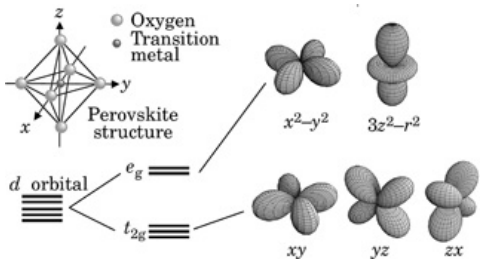

Figure 2.2: Crystal field splitting of the transition metal d-orbital due orbital overlap with a surrounding oxygen octahedra. Reused from [60].

Further splitting of the energy levels occur due to the Jahn-Teller distortions, which is a geometrical distortion of the oxygen octahedra. In manganites the distortion happens through elongation or compression of the oxygen octahedron along the c-axis, compensated by compression or elongation along the a and b axes[60].

The strength of the Jahn-Teller effect depends on the filling of the e_g and t_{2g} orbitals. If there is for example one electron in the t_{2g} level, say d_{xy}, the energy can be lowered by stretching the octahedral in the xy-plane and compressing it along the z-axis. On the other hand, no Jahn-Teller distortions will occur if the three t_{2g} orbitals are filled with one electron each.

2.2.2 Charge Transport in Manganites

In the core of understanding the transport properties of doped manganites is the double exchange mechanism proposed by Jonker and Van Santen in 1950. They observed a strong correlation between the metallic conductivity and ferromagnetism in doped manganites[61]. The transition from ferromagnetic to paramagnetic happened at about the same temperature as the transition from metallic to insulating. The connection can be explained by the interaction between different valence Mn ions.

First, the valence of Mn ions in doped LSMO is a combination of 3+ and 4+ and with electronic structure $[Ar]3d^4$ and $[Ar]3d^3$, respectively. The electrons will be distributed among the t_{2g} and e_g sublevels of the five 3d levels, as illustrated in figure 2.3a. For the 4+ oxidation state the three electrons will fill the three orbitals in the t_{2g} level with spin up configuration. The 3+ oxidation state has an additional electron that need to go into one of the free orbitals. This can be done either by occupying the lowest t_{2g} orbital in spin down state, or occupy the lowest of the e_g orbital in the spin up state. Because of strong Hund ferromagnetic coupling J_H, the fourth electron goes in the state that is aligned with the three t_{2g} electrons, which is the e_g orbital with spin up.

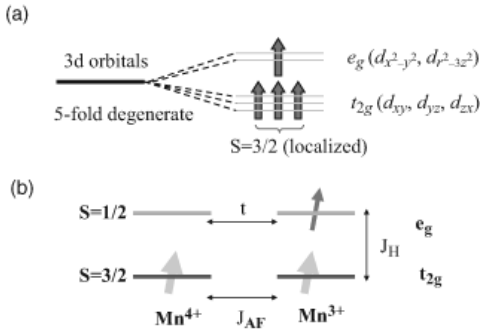

Figure 2.3: Double exchange mechanism in doped perovskite manganites. The e_g electron in Mn^{3+} can tunnel to a neighboring Mn^{4+} ion through an intermediate oxygen ion with an tunneling amplitude t. Because tunnelling conserves the electorn spin, and a strong Hund coupling J_H exist between the e_g and t_{2g} spins, alignment of the spins is energetically favorable at certain doping concentrations. Reused from [60].

Secondly, consider bringing two Mn ions of different valency together as illustrated in figure 2.3b. There are three magnetic exchange effects observed in this situation. First, the spin in the t_{2g} levels of the two Mn ions will couple antiferromagnetically through Heisenberg interactions with the strength J_{AF}. Then, the Mn 3+ ion the e_g electron couple ferromagnetically to the t_{2g} electrons in the same ion with strength J_H. Finally, the e_g electron has the possibility to tunnel from the Mn^{4+} to the Mn^{3+} ion, thereby lowering the energy by delocalization. This tunneling effect is called the double exchange (DE) mechanism, and is mediated by the intermediate oxygen ion. Because tunneling conserves spin, the tunneling amplitude is maximized if the spins of the Mn ions are aligned. This way the DE favors FM alignment, and directly competes with the AFM coupling of the t_{2g} spins. Now, the relative strengths of each of these interactions and the relative amounts of Mn^{4+} and Mn^{3+} ions in the material determines what magnetic ordering is energetically favored.

We will look at two extreme level of doping, $x = 0$ and $x = 1$, and then what happens in between. If there is no doping the DE is suppressed, since there are no free states for the e_g electron to tunnel to. This explains why LMO is AFM and insulating. At the other extreme of doping, where all La is replaced with Sr, there are no longer any e_g electrons, and no DE can occur. Therefore, SMO is AFM and insulating. As the level of doping is increased from $x = 0$, at some point the energy gain of delocalizing the e_g electron becomes larger than the energy gain from AFM-alignment of the t_{2g} spins, resulting in alignment of the t_{2g} spins and conductive material. If the doping is increased further, the number of e_g electrons, and consequently also DE, is reduced. This reduces the energy gain of delocalization and promotes AFM ordering.

2.2.3 Colossal Magneto Resistance

Doped manganites with metallic ferromagnetic ground states have an unconventional resistivity versus temperature curve[52, 62], such as the one for $La_{1-x}Ca_xMnO_3$ in figure 2.4. Above the magnetic ordering temperature the resistivity show insulating characteristics, with resistivity increasing when the temperature is lowered. At the ordering temperature the resistivity has a sharp peak. Below the ordering temperature the resistivty follows metallic behavior, showing a reduction in resistivity with temperature. By applying an external magnetic field of a few tesla, the resistivty peak at the ordering temperature is rapidly suppressed, showing the CMR effect.

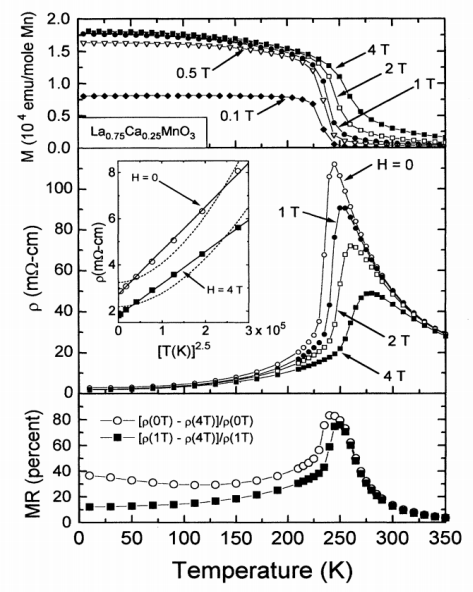

Figure 2.4: CMR in $La_{0.75}Ca_{0.25}MnO_3$. The figure show the evolution of magnetization, resistivity and magnetoresistance with temperature at different strengths of applied magnetic field. Reproduced with permission from [52]

The physics behind CMR has been discussed for decades, with the current understanding based on phase competition. Sophisticated computer simulations including the DE mechanism and coupling with Jahn-Teller lattice displacements show characteristics resembling the CMR in manganites[63]. DE alone is not sufficient to explain the magnitude of the CMR [64], but a qualitative explanation gives an intuitive understanding of how double exchange contributes to the CMR. At temperatures close to T_C, the magnetization decreases as the spins become less aligned. The reduced alignment reduces electron hopping, which results in increased resistivity. An external magnetic field can realign the spins, thus promoting electron hopping and reducing resistance.

The magnitude of the CMR is quantified by the ratio of the change in resistivity in the applied magnetic field. There are several conventions in literature on how to write the CMR ratio. We will use the change in resistivity $R(0) - R(H)$ over the resistance in the applied field $R(H)$

$$MR_H = \frac{R(0) - R(H)}{R(H)} \tag{2.1}$$

With this convention the CMR ratio becomes positive if the applied field reduces the resistance.

2.2.4 Optimally Doped LSMO

For doping level of $x = 0.3$ LSMO is ferromagnetic and a half metal with T_C of 370 K. At this doping level the magnetic ordering and conductivity are explained by the DE mechanism [65]. The material is nearly 100 % spin polarized[66], which is explained by a band gap in the density of states at the Fermi level for the minority spin.

2.3 Barium Titanate

$BaTiO_3$ is a ferroelectric material with the perovskite structure. It is used as the ferroelectric material in the heterostructures in this study, thus a short overview of given. Since its discovery more than sixty years ago, BTO has become the most widely used ferroelectric material, with applications in multilayer capacitors, piezoelectric transducers, thermistors and more[67, 68].

The basic structure of BTO is the centrosymmetric perovskite ABO_3, with Bi^{2+} at the corner A-site, Ti^{4+} in the center B site, and O^{2-} in the face centers[67, 69]. BTO show three distinct phase transition, as illustrated in figure 2.5. Starting at high temperature and going down, BTO goes through a cubic to tetragonal transition at 393 K, followed by a transition to monoclinic at 278 K, and then to rhombohedral at 183 K[33]. The change in unit cell parameters breaks the symmetry and gives the ferroelectricity observed in BTO, where the central Ti^{4+} is displaced, giving a polarization of the material. Under the application of an external electric field, the displacement of Ti^{4+} can be switched, thereby reversing the polarization.

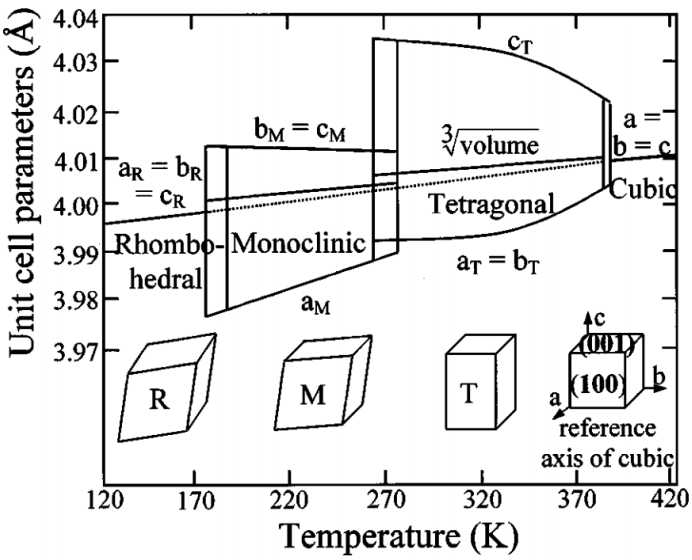

Figure 2.5: Phase diagram for $BaTiO_3$ and evolvement of unit cell parameters. Starting from the cubic high temperature state, BTO goes through three phase transition to tetragonal (T), monoclinic (M) and rhombohedral (R). Reproduced from [33].

2.4 Multiferroic Materials

In the last decade research has flurried on the topic of multiferroics, which are materials that simultaneously exhibit more than one ferroic order, such as antiferromagnetism, ferromagnetism and ferroelectricity[70]. The goal is to create new multifunctional devices where magnetism and electricity are coupled, such that control of one gives control of the other. This way, applied magnetic fields can be used to control charges, and electric fields to control spins, through the magnetoelectric effect (ME).

2.4.1 Magnetoelectric Effect

In mathematical form, the ME effect allows control of electric polarization $\mathbf{P(H)}$ with an applied magnetic field $\mathbf{H}$, or control of magnetization $\mathbf{M(E)}$ with an applied electric field $\mathbf{E}$.

Multiferroic ME materials can be divided into single-phase systems and two-phase systems[71]. At first, research on multiferroic materials was aimed at finding both ferroelectricty and magnetism in one material[72]. However, this proved to be challenging because the required parameters for the two phases are mutually

exclusive. The conventional mechanism for ferroelectricity is based on cation off-centering, which formally requires an empty d-orbital. On the other hand, ferromagnetism is usually observed in materials with ions with partially filled d-orbitals. Routes exist for creating single phase multiferroic materials, such as the perovskite $BiFeO_3$ where the A-site cation provide ferroelectricity and the smaller B-site cation is magnetic[71, 73]. Today, reseach is shifted towards multi-phase compounds, such as thin-film heterostructures, where one phase is ferroelectric and the other ferromagnetic[raa,59].

The traditional way of describing the ME effect in single phase crystals is with Landau theory with the free energy F of the system depending on the magnetic field $\mathbf{H}$ and electric field $\mathbf{E}$, with i-th components H_i and E_i. An expansion of the free energy of the material gives[74]

$$\begin{aligned} F(E,H) =& F_0 - P_i^S E_i - M_i^S H_i - \frac{1}{2}\epsilon_0\epsilon_{ij}E_iE_j - \frac{1}{2}\mu_0\mu_{ij}H_iH_j \\ & - \alpha_{ij}E_iH_j - \frac{\beta_{ijk}}{2}E_iH_jH_k - \frac{\gamma_{ijk}}{2}H_iE_jE_k - ... \end{aligned}$$

where P_i^S and M_i^S are the spontaneous polarization and magnetization, ϵ_0 is the permittivity of free space and ϵ_{ij} is a second rank tensor describing the relative permittivity. The magnetic permeability of free space and relative permeability are μ_0 and μ_{ij}, respectively. The fourth term describes the electric response from the electric field, while the fifth term describes the magnetic response from a magnetic field. The sixth term describes the linear magnetoelectric effect, where a_{ij} is the ME coupling factor. The final terms describe higher order terms parameterized by β_{ijk} and γ_{ijk}.

By differentiating the free energy with respect to electric field E_i the polarization is

$$\begin{aligned} P_i(\mathbf{E},\mathbf{H}) &= -\frac{\partial F}{\partial E_i} \\ &= P_i^S + \frac{1}{2}\epsilon_0\epsilon_{ij}E_j + \alpha_{ij}H_j + \frac{1}{2}\beta_{ijk}H_jH_k + \gamma_{ijk}H_iE_j - ... \end{aligned} \tag{2.2}$$

and for magnetization

$$\begin{aligned} M_i(\mathbf{E},\mathbf{H}) &= -\frac{\partial F}{\partial H_i} \\ &= M_i^S + \frac{1}{2}\mu_0\mu_{ij}H_j + \alpha_{ij}E_i + \frac{1}{2}\beta_{ijk}E_iH_j + \frac{1}{2}\gamma_{ijk}E_jE_k - ... \end{aligned} \tag{2.3}$$

By ignoring the higher order terms and setting E_j and $H_i = 0$ the following relations are obtained

$$\begin{aligned} \Delta P_i &\approx \alpha_{ij} H_j \\ \Delta M_j &\approx \alpha_{ij} E_i \end{aligned} \tag{2.4}$$

The ME coupling factor α_{ij} is taken as a measure of the coupling strength, and is normally given with the SI units sm^{-1}. The magnetoelectric voltage coefficient, $\alpha_E = \partial E/\partial H$ with units $Vcm^{-1}Oe^{-1}$ is also common.

When ferroelectric and ferromagnetic thin films are combined in a heterostructure, a multiphase multiferroic material may be obtained. On their own, neither of the phases are multiferroic, but the interaction between the phases may lead to an extrinsic ME effect.

2.5 The Hall Effect

In this section background and theory for the Hall effect is presented, and will later be used for characterization of the nanostructured devices fabricated in this work. The Hall effect is a classical correction to the conductivity and resistivity tensors when magnetic fields are introduced, and can be used to determine the sign of the charge carriers, the charge carrier density and mobility. It was first observed by E.H. Hall in 1879 [75], and is used today in sensor technology [76] and electronic transport characterization of conductive materials.

2.5.1 Simple Model

The fundamental physics of the Hall effect can most easily be illustrated with a one band model. The model describes well what is observed in simple metals with a spherical Fermi surface and semiconductors where one type of charge carrier is dominant [77].

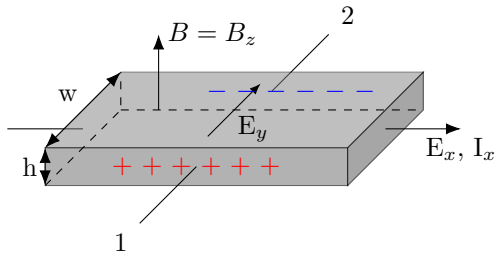

Figure 2.6: The Hall effect can be observed when charges move in a conductor that is in a magnetic field. The simplified case of a uniform magnetic field B_z along the z-axis and an applied electric field E_x along the x-axis for positive charge carriers is illustrated here. The magnetic field gives a deflection of the charge carriers moving in the x-direction, resulting in an accumulation of charge and the build up of a transversal electric field E_y. If the majority carrier is holes (electrons) a build up of positive (negative) charge at side 1. The voltage between side 1 and 2 is the Hall voltage V_H.

The forces on a charged particle moving through an uniform magnetic field is described by the Lorentz force

$$\mathbf{F} = q(\mathbf{E} + \mathbf{v} \times \mathbf{B}) \tag{2.5}$$

where q is the charge, $\mathbf{E}$ is the electric field, $\mathbf{v}$ is the velocity vector of the particle and $\mathbf{B}$ is the magnetic field. Figure 2.6 illustrates charged particles moving through a conductive slab with thickness t and width w by an applied electric field E_x in the x-direction. The moment a magnetic field B_z is turned on along the z-axis, the force on the moving charges can be written as

$$F_x = q(E_x + v_y B_z) \tag{2.6}$$

$$F_y = -qv_x B_z \tag{2.7}$$

$$F_z = 0 \tag{2.8}$$

The magnetic field gives deflection of the charge carriers moving in the x-direction, resulting in an accumulation of charge and the build up for a transversal electric field E_y. If the majority carrier are holes (electrons) there will be a build up of positive (negative) charge at side 1.

In a steady state situation the current in the y direction must be zero, since no current can flow out of the rod. This implies that the transverse electric field E_y balances out the force generated by the magnetic field

$$E_y = v_x B_z \tag{2.9}$$

The transverse electric field is treated as uniform across the interior of the device for the above relation is to hold. It follows that an electrostatic potential is established with the magnitude

$$V_H = E_y w = v_x B_z w \tag{2.10}$$

The potential, V_H is known as the Hall voltage. In an experiment I_x is a quantity that can be directly measured and is related to the carrier density n and drift velocity v_x by [77]

$$I_x = nqv_x A \equiv v_x = \frac{I_x}{nqwt} \tag{2.11}$$

where $A = wt$ is the cross-section area and t the thickness. By substituting v_x in equation (2.10) with (2.11) gives

$$V_y = \frac{I_x}{nqt} B_z \tag{2.12}$$

which can be rearranged to give an expression for the carrier density n

$$n = \frac{I_x B_z}{q V_y t} \tag{2.13}$$

or with sheet carrier density

$$n_s = nt = \frac{I_x B_z}{q V_y} \tag{2.14}$$

An interesting quantity to look at is the relation between the built up field and the current and magnetic field. The Hall coefficient is defined as [77]

$$R_H = \frac{E_y}{j_x B_z} \tag{2.15}$$

The value of the hall coefficient can be determined in an experiment when the dimensions of the sample is known. Replacing E_y with 2.9 and current density with the product of carrier density, charge and velocity $j_x = nqv_x$ gives

$$R_H = \frac{1}{nq} \tag{2.16}$$

The sign of the Hall Coefficient reveals the carrier type and the magnitude gives the carrier density. If the majority charge carrier are electrons (holes) the coefficient is negative (positive). Hall measurements can therefore be very useful when determining the carrier type and density of metals and doped semiconductors.

A final important transport property that can be determined using the results from Hall measurements is the mobility. The relation between resistivity ρ and mobility μ for materials with excess of one carrier type is:

$$\rho = \frac{1}{nq\mu} \tag{2.17}$$

Substituting ρ and n for the sheet resistance $R_s = \rho/t$ and sheet carrier density $n_s = n/t$, respectively, gives the following relation

$$\mu = \frac{1}{qn_sR_s} \tag{2.18}$$

Finally, by inserting the sheet carrier density from equation (2.14) in (2.18) gives

$$\mu = \frac{V_H}{R_sI_xB_z} \tag{2.19}$$

where all the quantities can be determined experimentally using a Hall bar geometry.

2.5.2 Two charge carriers

In the situation where both electrons and holes contribute to the conductivity the simple one band model is not valid. Adjustments to the current density gives a new set of equations for the hall coefficient and mobility. If holes and electrons are treated as moving in different bands without interacting the current density is

$$j = qn_ev_e + qn_hv_h = q(n_e\mu_e + n_h\mu_h)E \tag{2.20}$$

where $n_{e,h}$ is the density, $v_{e,h}$ the velocity and $\mu_{e,h}$ the mobility for electrons and holes respectively. Using the definition of resistivity as the ration of electric field to current density [78] together with equation (2.20) gives

$$\rho = \frac{1}{q(n_e\mu_e + n_h\mu_h)} \tag{2.21}$$

The equation for the Hall Coefficient with two charge carriers is [79]

$$R_H = \frac{n_h \mu_h^2 - n_e \mu_e^2}{q(n_h \mu_h + n_e \mu_e)^2} \tag{2.22}$$

In materials with two charge carriers it is not sufficient to perform only hall measurements. The sign and magnitude of the hall coefficient cannot be directly used to determine the carrier type and concentration. To calculate the concentration of holes and electrons the ratio of electron to hole mobility μ_e/μ_h must determined.

2.5.3 Anomalous Hall Effect

Following the discovery of the Hall effect, Edwin H. Hall observed in 1881 that the effect was ten times larger in ferromagnetic iron [80] than in non-magnetic conductors. This was the first observation of what is known today as the anomalous Hall effect (AHE).

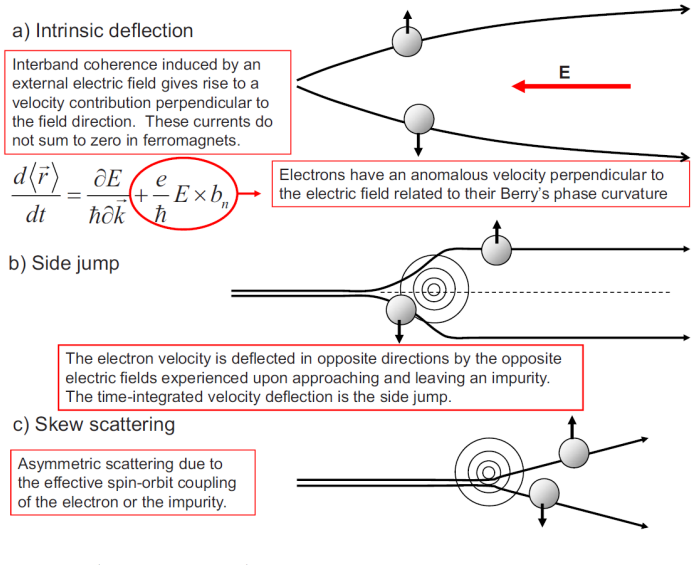

Figure 2.7: The three main mechanism behind AHE. From [81]

The dependence of the Hall resistivity ρ_{xy} on applied magnetic field H_z behaves fundamentally differently in ferromagnetic and nonmagnetic conductors. Pugh and Lippert established an empirical relation between ρ_{xy}, the applied magnetic field H_z, and the magnetization of the sample M_z [82]

$$\rho_H = R_0 H_z + R_s M_z \tag{2.23}$$

where R_s describes the contribution from the AHE. From this equation it is obvious that the AHE saturates when the medium is totally magnetized.

The first explanation of the anomalous hall effect was given by Karplus and Luttinger in 1954 [83]. They observed that the application by an external electric field to the solid may contribute to the group velocity of the electrons. It was found that in conducting ferromagnets the alignment of spin would cause the mean anomalous group velocity to be nonzero and perpendicular to the electric field, giving a net contribution to the Hall conductivity. The current is proportional to the degree of magnetization, and saturates when all spins are aligned. The effect depends only on the band structure of the material and is referred to as an intrinsic contribution to the AHE.

A second contribution to the AHE was identified by Smit [84, 85] and is based on the asymmetrical scattering of electrons with impurities. This extrinsic mechanism is named skew scattering, and is proportional to the Bloch state transport lifetime. Because of this the effect dominates in nearly perfect crystals where the lifetime is long.

The third contribution is the side jump model proposed by Berger [86]. The side jump model considers the scattering of a Gaussian wave packet from a spherical impurity. These three main contributions to the AHE are summarized in figure 2.7.

2.5.4 Hall Effect in Manganites

Asamitsu and Tokura investigated the effect of doping and temperature on the Hall effect in LSMO [87]. The study indicated that the carrier in LSMO at 4.2 K is a hole with a carrier density $n \approx 1$hole/Mn site, nearly independent of the doping level. They reported that the AHE in LSMO is negative and strongly doping and temperature dependent, with anomalous Hall coefficient scaling with 3/2 power of the change in magnetization and independent of doping level.

A study by of the Hall effect in thin films of $(La_{1-y}Gd_y)_{0.67}Ca_{0.33}MnO_3$ found a negative charge carrier sign in the paramagnetic region, indicating that charge transport is dominated by the DE electron hopping mechanism[88].

Measurements of the Hall effect on $La_{1-x}Ca_xMnO_3$ films found a carrier density in the ferromagnetic phase of $n \approx 1$hole/Mn site, which changed to electron-like near T_C.

A different study of $La_{0.67}(Ca,Pb)_{0.33}MnO_3$ also showed a negative anomalous Hall effect contribution, but attributed it to skew scattering. The AHE in manganites have been observed to saturate at high fields or temperature, an attribute that can be exploited to investigate the ordinary Hall effect.

Chapter 3

NANOSTRUCTURING

This chapter will go through the relevant nanostructuring techniques used in this work. First, nanostructuring by electron beam lithography will be presented. Next, thin film patterning by spin coating and physical vapor deposition is covered. Then, the final section covers pattern transfer at the nanoscale.

3.1 Nanofabrication with Electron Beam Lithography

In this section nanostructuring with electron beam lithography(EBL) is covered. First, a basic introduction to EBL is given. Then, theory on electron optics, scattering and proximity effect is given.

Theory in this section is mainly based on chapter 3 in Nanofabrication by Cui[89].

3.1.1 Introduction

In the EBL a finely focused electron beam is moved across a sample to selectively expose a thin electron sensitive polymer known as a resist. The electrons cut the polymer into shorter segments by chain-scission, making the exposed area more sensitive for dissolving in a solution called the developer[1].

The first EBL systems appeared in the early 1960 after the discovery of the electron sensitive material PMMA[90] and were usually based on modified scanning electron microscopes (SEM). EBL is not limited by the diffraction limit observed in optical lithography, which allowed researchers to establish structures much finer then before. In 1970s EBL intruments were able to pattern structures down to 60 nm[91]. With the state-of-the-art EBL instruments today patterns smaller than 10 nm can be produced [92].

EBL has become a cornerstone for nanoscale research because it allows quick prototyping with sub-100nm resolution. However, for volume manufacturing of integrated circuits EBL is fundamentally handicapped due to the low throughput associated with direct writing, and cannot compete with the parallel projection of photons in optical lithography.

[1]This is true for a positive resist such as PMMA. For negative resists the opposite is true, where exposed area becomes less soluble in the developer

3.1.2 Electron Beam Optics

The high resolution capabilities of EBL is enabled by the small beam spot that can be achieved with electron optics. Electron optics use magnetic and electronic fields to exert forces on the electrons, as described by the Lorenz force in eq. (2.5).

Magnetic lenses are commonly used in EBL systems because they offer high focusing power. The magnetic field is generated by passing high currents through a set of coils, thereby generating a rotationally symmetric magnetic field inside the coil. The magnetic field strength is radially inhomogeneous, and the strength increases with the distance from the center. In that way, electrons that enter the lens off-center are deflected more than the one passing closer to the center axis, thereby generating a focused beam.

The beam spot focused by the electron optical system is an image of the electron source. Therefore, to achieve a small beam spot the electron source should be small. The most commonly used source in EBL systems today is the Schottky Field Emission (FE) source, which is a very fine needle where electrons are extracted from the tip by a strong electrical field. Schottky FE sources have low beam noise and emission current drift, which are both necessary in EBL where a consistent exposure dose is needed.

3.1.3 Aberrations

The electron optics in between the source and the sample introduce aberrations that affect the final beam size. To minimize the beam size, the aberrations must be kept at a minimum. Electron beam optics have geometrical aberrations, such as spherical aberration and astigmatism, and non-geometrical aberrations, such as chromatic aberration.

A schematic of a typical electron optical system in an EBL column can be seen in figure 3.1[92]. The electron gun assembly sits at the top, and includes the source and a set of lenses and aperture to initially focus the beam. Then, the condenser lens further focuses the beam, followed by a beam blanker that can be used to switch the beam on or off. Next, a selectable aperture is used to block electrons moving off-center. A set of deflectors are used scan the beam, while a final objective lens focuses the beam on to the surface of the sample.

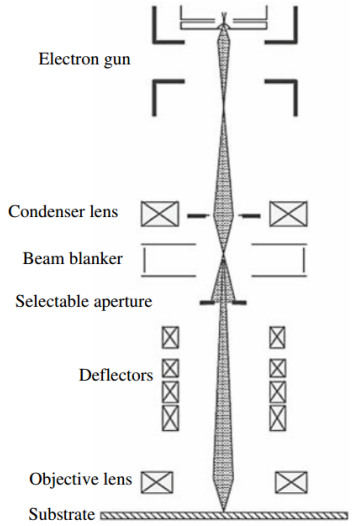

Figure 3.1: Schematic of a typical electron optical system in an EBL column. From [89], originally [92]

The beam spot on-axis at the surface of the sample, with aberrations included, can be expressed with [93]

$$d = \sqrt{d_g^2 + d_s^2 + d_c^2 + d_d^2} \tag{3.1}$$

Where d_g is the beam spot without aberrations, d_s is spherical aberration, d_c is chromatic aberration and d_d is the diffraction limit. The magnitude of spherical aberrations is given by the following formula

$$d_s = \frac{1}{2} C_s \alpha^3 \tag{3.2}$$

Where C_s is chromatic aberration coefficient and α is the beam convergence angle. The design of the electron optical system can be used to minimize the chromatic aberration coefficient. However, the most effective way to reduce chromatic aberrations is to reduce the beam convergence angle, since the aberration is proportional to the cubic power of it. This can be done by inserting a smaller aperture. The magnitude of chromatic aberrations is given by

$$d_c = C_c \alpha \frac{\Delta V}{V} \tag{3.3}$$

Where C_c is chromatic aberration coefficient, ΔV the beam energy spread and V the beam energy. Chromatic aberrations are reduced with smaller beam

convergence angle and higher acceleration voltage. The energy spread originates from the electron source and instability in the applied current in the magnetic lenses, and are not easily controlled. The magnitude of the diffraction limit is given by

$$d_d = 0.6\frac{\lambda}{\alpha} \tag{3.4}$$

Where $\lambda = \frac{1.2}{\sqrt{V}}$nm is the electron wavelength. While the spherical and chromatic aberrations are reduced if the convergance angle is reduced, the effect is the opposite on the diffraction aberrations. Increasing the beam energy can be done to reduce the diffraction effect.

Another effect that contribute to the aberrations when using electron optics is the space charge effect. At the points in the column where the beam is focused into a small point, the high density of charges result in Coulomb repulsion forces. This leads to increase in both the energy spread and the diameter of the beam[94]. The space charge effect can be reduced by lowering the beam current, but in an EBL this comes at the cost of increased exposure time.

The space charge effect can be reduced by increasing the beam energy. Increased beam energy also reduces chromatic aberrations and the diffraction limit, and this is the reason why most advanced EBL systems operate at 100 kV acceleration voltage. Aberrations associated with the beam deflectors have not been accounted for in the above description. The aberrations from beam deflectors are mainly distortions and astigmatism that scale with the cubic power of the distance of deflection off-center. Because of this, the sample should be positioned so that small features are close to the center of the column.

3.1.4 Scattering

Achieving high resolution in EBL requires not only a highly focused beam. The interaction volume of the electron beam with the sample must be also accounted for. The high energy electrons in the beam are called primary electrons, and penetrate the surface of the sample and scatter on the atomic nucleus and the surrounding electrons. When the primary electron passes close by the atomic nucleus, coulomb attractions between the positively charged nucleus and the negatively charged electron causes the electron to deflect towards the nucleus. The closer the electron passes the nucleus the stronger is the deflection. This gives elastic scattering of the primary electrons. Small angle scattering is called forward scattering, while large angle scattering is called backscattering.

As the primary electron moves through the material, inelastic scattering knocks out secondary electrons from the solid. The secondary electron can have energies up to several keV, which is enough to knock out additional electrons in the resist.

This sets of a chain reaction, where the resist is cut into shorter segments by chain-scission. The secondary electrons have an initial momentum in the direction perpendicular to the primary electron. The secondary electron thus contributes to broadening of the exposure area. A secondary electron with 400 eV energy will travel about 12 nm before it comes to rest[95].

The true interactions between the electrons and the material is described by energy fields, and can be modeled by Monte Carlo simulations[96, 97]. It is a numerical technique that can be used to solve mathematic equations with a random process. The scattering process of primary electrons is a random process, since it cannot be predicted what direction the electron will scatter and how far it is between each scattering event. Mathematical descriptions of the probabilities of elastic and inelastic scattering can be used as input to the simulations[98]. The simulated trajectory of two primary electrons in 0.1 µm PMMA on silicon can be seen in figure 3.2. To generate a statistically correct result, over 50000 electrons must be included in the simulations.

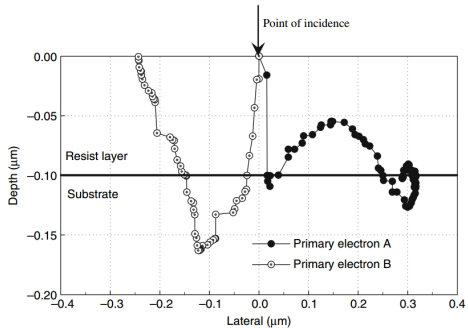

Figure 3.2: Monte Carlo simulation of trajectories of two primary electrons scattering in PMMA on Si. From [89]

The outcome from the Monte Carlo simulations of the scattering can be used to generate point spread functions (PSF), where the energy deposited by the beam in the resist is plotted as function of lateral distance from the point of incidence. Such PSF plots can be used to reveal factors that strongly influence the electron scattering.

Three factors that strongly influence electron scattering are electron energy, density of substrate material and resist thickness. Firstly, primary electrons with high energy have a smaller scattering angle, which results in more low angle scattering and less broadening of the beam. Figure 3.3a shows the PSF for electron energies of 50, 70 and 100 keV. Significantly less broadening is observed at higher energies. The reduced broadening is another reason why high energy electrons are preferred in EBL.

Secondly, more electrons will backscatter from a substrate of high density. Figure

3.3b compares the PSF of Si with GaAs, which is about 2.3 times denser than Si. The PSF for GaAs is broader than that of Si, which is why low density substrates such as Si is preferred for high resolution EBL.

Finally, the resist should be thin for high resolution EBL. Figure 3.3c show the PSF at different depth in the resist. The PSF is broader in the bottom of the resist than at the top, which is due to forward scattering of electrons as they go deeper in the resist.

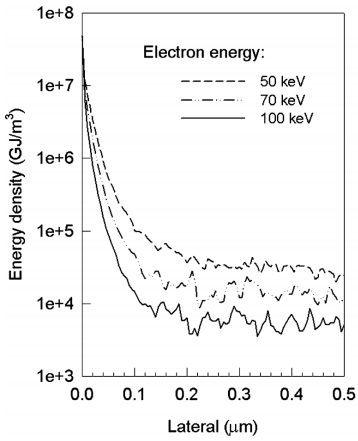

(a) PSF for different beam energy

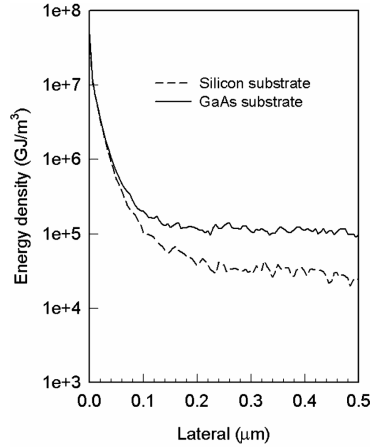

(b) PSF for different substrate material

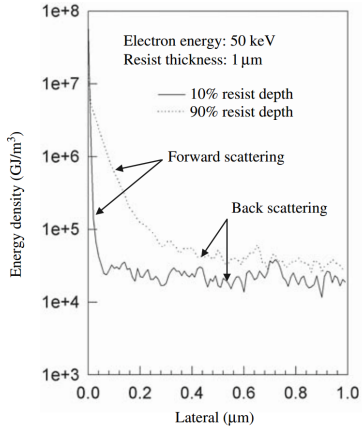

(c) PSF at different depth

Figure 3.3: Point spread functions of electron energy deposition in resist for (a) different beam energy, (b) different substrate material and (c) different depth in the resist. From [89].

3.1.5 Proximity Effect and Correction

Because scattering of electrons in EBL gives energy deposition in the proximity of the beam spot, dense features become overexposed and isolated features underexposed, and gives the so-called proximity effect.

Proximity effect correction is necessary for achieving high resolution EBL, and has been part of the development for more than 30 years[99]. The three principal correction methods are dose correction, pattern size compensation, and background exposure compensation. The most used method, which is the one used in this work, is dose correction, will be covered here.

The principle behind dose correction is to adjust the exposure dose at different parts of the pattern, with the goal of achieving equal exposure energy for all patterns. Figure 3.4a show a simple mask where all areas receive the same exposure dose. The simulated resist profile for this mask is seen in figure 3.4b. Due to scattering and the proximity effect, the lines between the two squares cannot be resolved. In figure 3.4c the different areas on the mask are given varying exposure dose, where lighter color indicate lower dose. The resulting resist profile can be seen in figure 3.4d, and show clearly resolvable lines.

The PEC in the example above is very simple, further improvements can be made by dividing the mask into even smaller sections. Computational methods have been developed that can self-consistently allocate doses for a pattern[99]. The method works by first assigning an equal dose to all of the areas, and using electron scattering to calculate the exposure energy on all of the patterns, and then make adjustments to the dose until the uniformity of the exposure energy is within a certain threshold.

3.1.6 Resist Materials and Processes

The energy of the electron beam has to be transferred into the resist material and initiate the chain-scission reaction to form the lithographic pattern.

The two most important properties of a resist is the sensitivity and the contrast. Sensitivity and contrast are derived from developer curves, which plot the remaining resist thickness as a function of exposure dose. A typical developer curve for positive resists can be seen in figure 3.5. The onset dose D_0 and the threshold dose D_1 are given by the intersection of the tanget at the steepest part of the curve with the original thickness and zero thickness lines respectively. The exposure dose at which the resist is completely developed to the bottom is defined as the sensitivity. A high sensitivity means that a low exposure dose is required to clear the resist. The contrast is related to the slope of the developer curve between points D_0 and D_1. The steeper the developer curve, the higher is the contrast.

For high resolution EBL a resist with low sensitivity and high contrast is preferred.

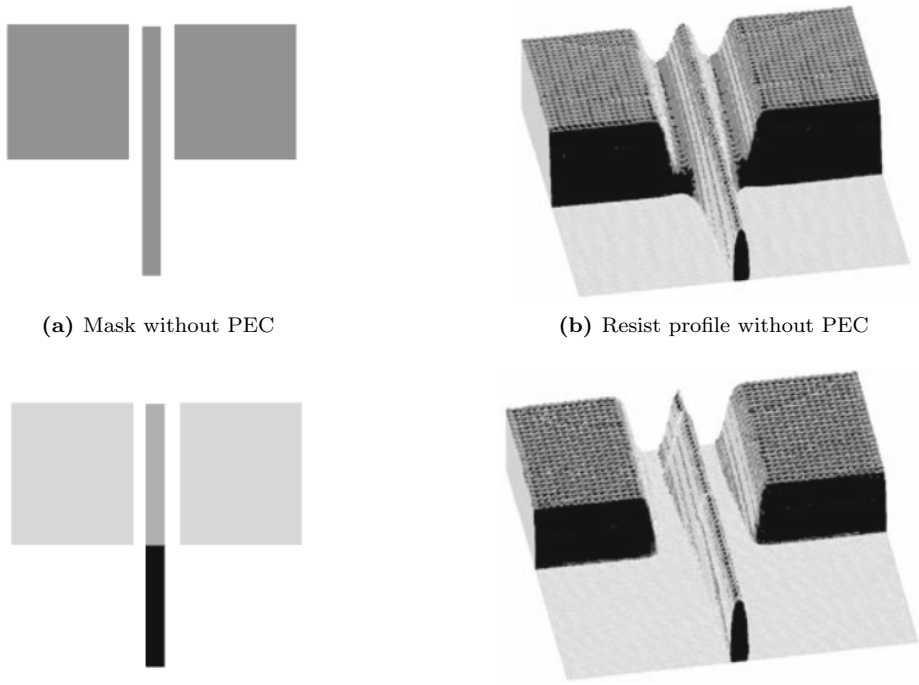

(a) Mask without PEC

(b) Resist profile without PEC

(c) Mask with PEC

(d) Resist profile with PEC

Figure 3.4: Effect of proximity effect dose correction on mask profile. Exposure pattern (a) with and (c) without proximity effect dose corrections, with resulting resist profile (b) and (d), respectively. From [89].

A low sensitivity resist will be less affected by the proximity effect, since more scattered electrons are needed to reach the onset dose. A drawback with using a low sensitivity resist is long write times, which generally limits the use to research and development projects.

Another factor in the EBL process is the developer chemistry. The standard developer for PMMA and MMA is methyl isobutyl ketone (MIBK) mixed with isopropanol (IPA). The sensitivity and resolution depends on the developer concentration as described in table 3.1. MIBK:IPA 1:3 offers the highest resolution and low sensitivity.

In some experiments, improvements in sensitivity, contrast and roughness have been observed for a co-solvent developer mixture of deionized (DI) water and IPA[100, 101].

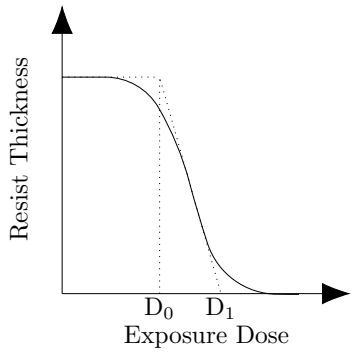

Figure 3.5: Typical developer curve for a positive resist

Table 3.1: Sensitivity and resolution of PMMA and MMA with MIBK:IPA as developer. Reproduced from [89]

Composition	Sensitivity	Resolution
MIBK:IPA 1:3	Low	Extremely High
MIBK:IPA 1:2	Medium	Very High
MIBK:IPA 1:1	High	High
Pure MIBK	Very High	Low

3.1.7 Conductivity of Sample

The conductivity of the sample is another critical factor when performing EBL, as well as other charged particle beam processes. A conductive path must be formed from the sample to ground to avoid charge build up from the beam. Charge build up will create a local electric field in the vicinity of the sample surface that deflects the incoming beam and blurs the image.

Non-conductive samples must be made conductive before EBL. There are several ways to make a sample conductive. The most straight forward is to evaporate a thin metallic layer on top of the sample before EBL. However, this is not always desirable, since the metallic layer may be hard to remove or it may react with the sample. Conductive resist have been developed, but this are seldom used due to high cost and short shelf life.

The effect of charging depends on both the beam current and the conductivity of the sample. To operate at high beam current, the sample should have low resistance to avoid charging. On the other hand, if the conductivity of the sample is poor, working at low beam current should reduce the charging effect.

3.2 Thin Film Deposition

In this section relevant thin film deposition techniques will be covered. The first section covers spin coating, which is used to apply the the resist layer before electron beam lithography. Then, two physical vapor deposition techniques are presented. First carbon coating by resistive heating, then metal deposition by electron beam evaporation.

3.2.1 Spin Coating

Spin coating is a technique for applying liquid polymer resist in a uniform layer[102]. Figure 3.6 illustrate the four main steps in spin coating. The steps involved in spin coating are

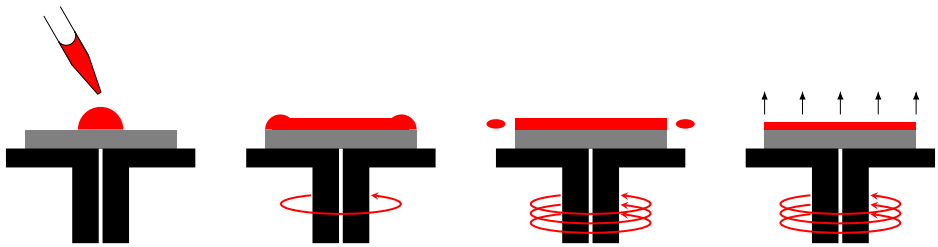

Figure 3.6: Illustration of spin coating process for depositing a uniform thin film of a liquid polymer resist. (a) A drop of resist is dispensed using a pipette. (b) The sample is accelerated to spread the resist over the surface. (c) Resist is quickly accelerated to high speed to throw off excess resist and form an uniform layer. (d) Sample continues to spin at constant speed while most solvent evaporate

Dispense The sample is placed in the center of the vacuum chuck and the polymer resist solution is applied using a pipette.

Spin-up The sample is accelerated to spread the resist over the surface of the sample

Spin-off Sample is accelerated to high RPM to throw off excess resist by centrifugal force and form an uniform resist layer

Solvent evaporation The sample continues to spin at constant speed until most of the solvent in the resist evaporates

The critical parameters that must be controlled for obtaining an uniform film with desired thickness are resist viscosity, spin speed, spin acceleration and spin time. The resist thickness is found to generally scale with the spin speed as

$$\text{Resist Thickness } \alpha \frac{1}{\sqrt{RPM}} \tag{3.5}$$

where RPM is revolution per minute. Each resist have a spin speed curve that can be used as a guideline to determine the final thickness. If the spin acceleration is slow, solvent will evaporate during the spin-up stage, which increases the viscosity of the resist and reduces uniformity. Hence, high spin acceleration is recommended.

3.2.2 Physical Vapor Deposition

Physical vapor deposition (PVD) is a group of techniques that use thermal heating or plasma sputtering under vacuum to produce thin films. Thermal evaporation can be divided into evaporation by electron beam or resistive heating. Table 3.2 show some of the characteristics of PVD methods.

Table 3.2: Characteristics of phyisical vapor deposition methods. Adapted from [89].

Technique	Material	Substrate Temperature	Directionality	Film density and uniformity
Resistive heating evaporation	Low melting point metals	$50 - 100\,^{\circ}\text{C}$	Good	Poor
Electron beam evaporation	High melting point metals and dielectrics	$50 - 100\,^{\circ}\text{C}$	Good	Poor
Plasma sputtering	Metals and dielectrics	$\approx 200\,^{\circ}\text{C}$	Moderate	Good

3.2.3 Electron Beam Evaporation

E-beam evaporation can be used to deposit thin films of metals, oxides, magnetic materials and dielectrics. Figure 3.7 shows the general layout of an e-beam evaporator. The sample is loaded on the top side of the chamber with the surface facing the evaporation source. The source is a crucible loaded with the material to be evaporated, and is heated by a high power electron beam. The electron beam is generated by a tungsten filament and steered onto the source using a magnetic field. By maintaining a high vacuum in the evaporator, the evaporated atoms gains an increased mean free path. This allows the evaporated atoms to travel in a straight path in the chamber until they reach the sample and condense.

With e-beam evaporation material deposit only on the part of the sample that face the evaporation source. If the sample have features with sharp, vertial edges, the thin film will deposit in the bottom of the trench and on the top, but not on the

sidewall, resulting in poor step coverage (See figure 3.8a). This property has led to the demise of e-beam evaporation in modern integrated circuit manufacturing where features need to be uniformly filled. An illustration of the good step coverage of sputter deposition can be seen in figure 3.8b. However, in certain research techniques the poor step coverage of e-beam evaporation is beneficial. This will be covered more in section 3.3.2 on lift off.

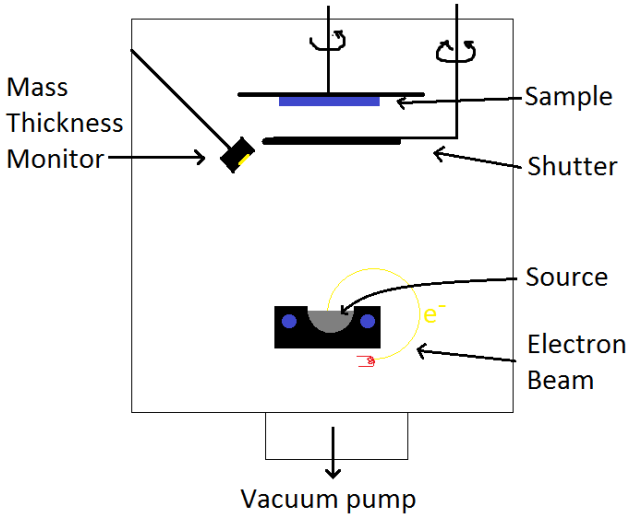

Figure 3.7: Schematic of E-beam evaporator tool. The sample is loaded facing downwards on a stage in the top of the chamber. An electron beam irradiates and heats the source up to the evaporation temperature. Evaporated atoms from the source travel in a straight path and deposit on the sample surface. Adapted from [89].

3.2.4 Carbon Coater

The carbon coater is an instrument intended for depositing thin carbon layers on non-conductive samples before SEM imaging and EDX-analysis. During the project work the sputter resistance for the carbon thin film was tested and found feasible for use as hard mask, with a sputter selectivity of about 1:1 compared to BTO and STO[49]. An important feature of the carbon thin film is that it does not react with the underlying oxide thin film. An additional desirable feature is that the remaining carbon can easily be removed using an oxygen plasma.

The carbon coater evaporates carbon at temperatures around 2400 °C in a vacuum of 10^{-4} mbar[103, 104]. A schematic of the instrument can be seen in figure 3.9. The sources are two carbon rods loaded with the flat ends in contact. One of the rods has a reduced diameter and is loaded on a spring so that connection

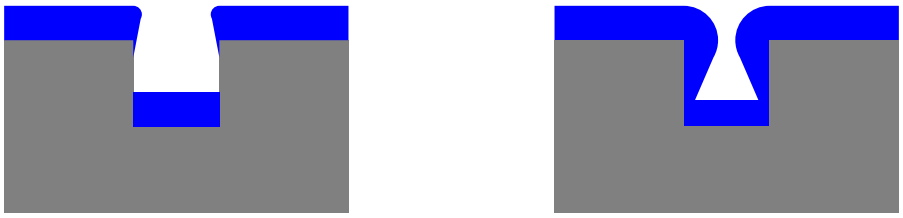

(a) E-beam deposition **(b)** Sputter deposition

Figure 3.8: Illustration of step coverage for (a) e-beam deposition and (b) sputter deposition. E-beam deposition gives poor step coverage, resulting in a discontiniuity in the deposited film. Sputter deposition has good step coverage, which gives a continious film.

is maintained while carbon is evaporated. The carbon rods are heated to the evaporation temperature by passing a high current through them, generating heat by electrical resistivity.

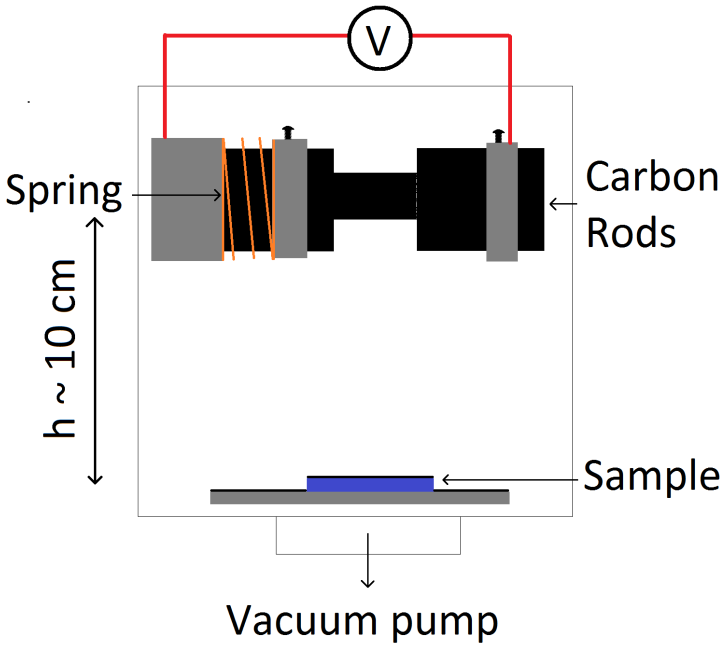

Figure 3.9: Schematic of Carbon Coater tool. Two carbon rods, one with reduced diameter, are brough in contact using a loaded spring. When passing a high current through the rods heat is generated at the constriction and gives evaporation of carbon.

3.3 Nanoscale Pattern Transfer

In this section nanoscale pattern transfer is covered. The focus will be on techniques that are used in this project.

The content of this section is mainly based on chapter 6 in Nanofabrication by Cui[89].

3.3.1 Introduction

The resist structured by EBL can be used as a mask to transfer the pattern to another material. Pattern transfer techniques are grouped in two main categories, additive processes and subtractive processes. In additive processes material is added by filling the open areas in the resist, while subtractive processes remove material exposed in the open area of the resist.

Three common pattern transfer processes can be seen in figure 3.10. The first (a) show a lift off process, which is an additive process where material is deposited through the opening in the resist. In figure (b) an subtractive process by etching into a thin film is shown, while figure (c) illustrate the subtractive process of etching into the substrate.

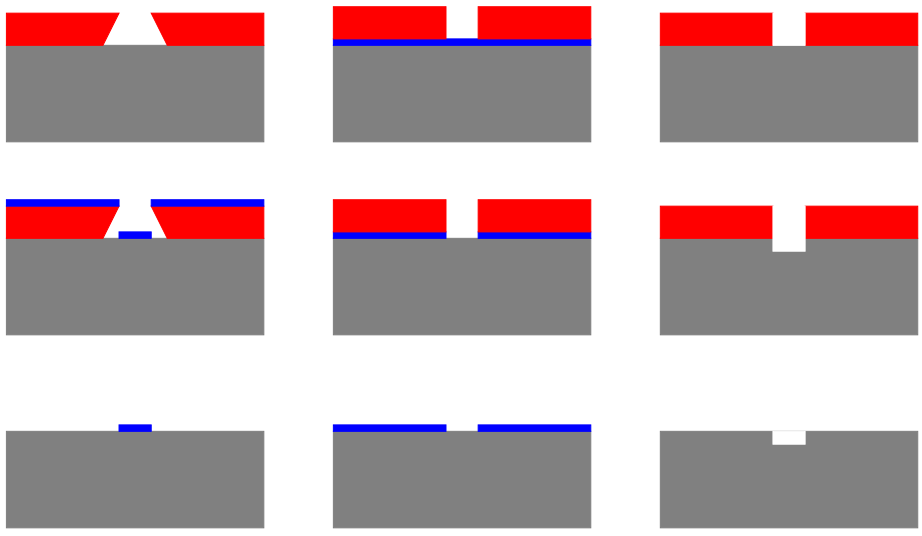

(a) Liftoff **(b)** Thin film etch **(c)** Substrate etch

Figure 3.10: Nanoscale pattern transfer. Adapted from [89]

3.3.2 Lift off

The concept of lift off was developed for more than 30 years ago, and has become the primary technique for patterning metallic thin films[105]. The process is illustrated in figure 3.10a. The first step is structuring of a resist layer with optical or electron beam lithography. Then, a metallic thin film is deposited on the patterned resist layer. In the next step the resist is dissolved in a wet chemical solution, and lifts off the metallic film on the top of the resist. This way, only the metallic thin film in direct contact with the substrate is left. The resolution of the lift off pattern transfer is in principle the same as that of the resist patterning process, and sub-10 nm lines have been demonstrated [106].

When performing lift off, PVD is preferred over other thin film deposition techniques, such as chemical vapor deposition, because the substrate temperature can be kept relatively low. During the thin film patterning process it is critical that the temperature of the substrate is below the glass transition temperature (T_g) of the resist. Above T_g the polymers are softened and become flowable, which leads to distortions at small dimensions. As can be seen in table 3.2, thermal evaporation methods have lower substrate temperature than plasma sputtering.

Another characteristic that must be considered is the directionality of the deposition technique. As can be seen in figure 3.10a, when performing additive pattern transfer by lift off, poor step coverage is required so that the thin film on top of the resist can be removed by dissolving the resist. Deposition by thermal evaporation is the most suitable for lift off because it has high directionality.

Reduced step coverage can be achieved using a thick resist. A rule of thumb is that the resist should be at least three times thicker than the thin film.

A desirable feature when performing lift off is to have an undercut profile in the resist. As described in section 3.1.4, scattering of electrons leads to an uneven energy deposition in the resist layer. As seen in figure 3.3c, the energy deposition becomes broader as the electrons go deeper in the resist. Monte Carlo simulations of the resist profile at various exposure doses can be seen in figure 3.11a, and show that an undercut can be achieved at 20 keV energy. The higher the exposure dose, the wider is the undercut. When aiming for high resolution EBL with thick resists a beam energy of 100 keV is preferred. However, at 100 keV it is hard to produce undercuts in the resist due to reduced forward scattering, as can be seen in figure 3.11b. Increasing the exposure dose is not an effective way to increase the undercut. For exposures at 100 keV a bilayer resist can be used to produce an undercut. This is done by having a bottom layer with much higher sensitivity than the top layer. A simulation of a high molecular weight PMMA top layer and low molecular weight copolymer bottom layer can be seen in figure 3.11c[89]. Both PMMA and the copolymer are sensitive to electron exposure, and are developed in the same solution. Hence, the undercut depends solely on the difference in sensitivity of the two layers.

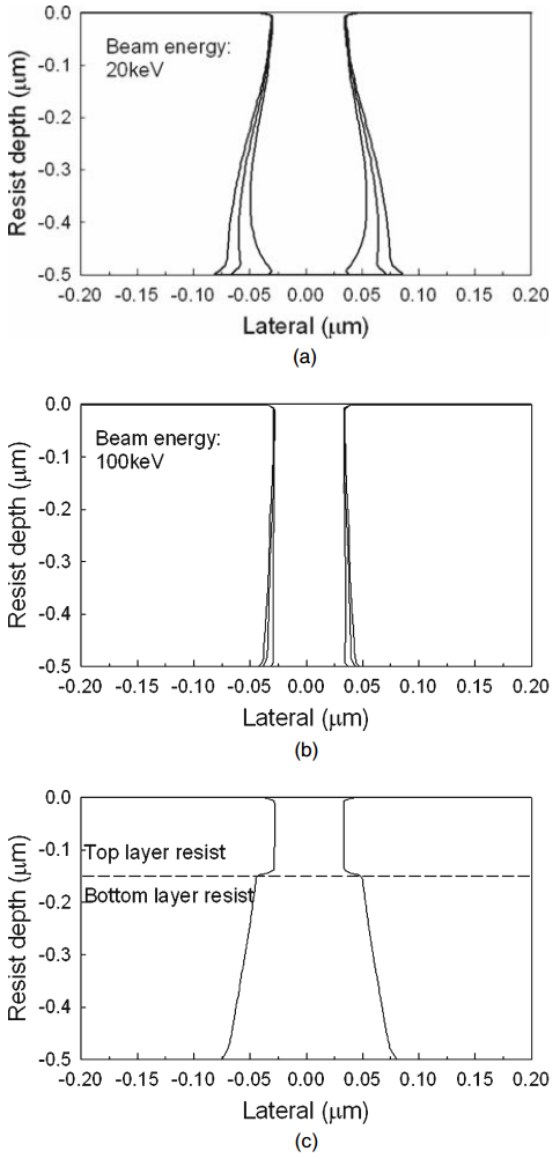

Figure 3.11: Monte Carlo simulations of undercut profiles by EBL. (a) Single layer PMMA resist exposed 20 keV beam energy at exposure doses of 100, 200 and 300 $\mu C\,cm^{-2}$. (b) Singe layer PMMA resist exposed at 100 keV beam energy at exposure doses of 300, 400 and 500 $\mu C\,cm^{-2}$. (c) Bilayer PMMA and copolymer at 100 keV beam energy at exposure dose of 300 $\mu C\,cm^{-2}$. From [89]

3.3.3 Etching

Etching techniques are used for subtractive pattern transfer, and can be divided into wet etching and dry etching. Wet etching uses etchant chemicals in liquid form. In dry etching the etchants can be in the form of gas or energized ions. The two main parameters that characterize an etching process are selectivity and anisotropy.

Selectivity is the ratio of substrate or thin film etching rate over mask etching rate. A high selectivity is desirable since it means that little of the mask is consumed in the etching process. When etching thin films, such as in figure 3.10b, a high selectivity between the thin film layer and substrate is preferred to avoid etching of the substrate.

Anisotropy is a measure of the directionality of the etching process. Because the purpose of the etching process is to transfer the mask pattern to the underlying material, an anisotropic etching process is preferred. Figure 3.12 illustrates the profiles of isotropic and anisotropic etching. Isotropic etching removes material in all directions, leading to increased lateral dimensions. This renders isotropic etching methods unsuitable for establishing most nanoscale or high aspect ratio features.

(a) Intial mask pattern

(b) Isotropic etch

(c) Anisotropic etch

Figure 3.12: Etching profiles for isotropic and anisotropic etch

3.3.4 Wet Etching

Wet etching methods are characterized as isotropic with high selectivity, and is in general not used for nanoscale pattern transfer. This is because the etchant liquid can penetrate underneath the mask by later etching, which results in a pattern larger than the mask opening, as illustrated in figure 3.12b.

Developing of resist is a form of anisotropic wet etching. The developer itself is isotropic, but anisotropy is achieved by the selectivity between the exposed and non-exposed resist.

3.3.5 Reactive Ion Etching

The most widely used dry etching technique is reactive ion etching (RIE)[107]. RIE involves both physical and chemical etching, and is characterized by high selectivity and anisotropy. The physical process in RIE involves generation of a plasma of reactive ion that sputter the samples surface.

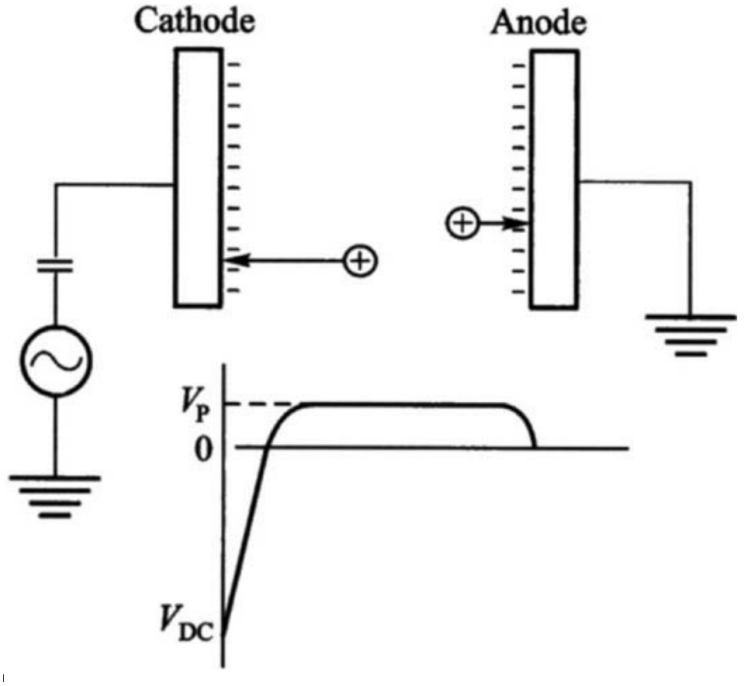

Figure 3.13: Schematic of parallel plate RIE. Distribution of electric potential is illustrated. From [89]

A schematic of a RIE in planar plate configuration can be seen in figure 3.13. One of the electrodes is a cathode and is connected to an RF power source via a capacitor. The other electrode is an anode, and it is directly coupled to ground. When the RF power source is turned on, an RF field is generated between the cathode and the anode. The frequency of the RF field is chosen so that it accelerates and resonates a small number of free electrons. A chain reaction starts when the free electrons collides with and ionizes the gas molecules. This ultimately leads to a transition of the space between the electrodes from insulating to conducting. The

potential distribution in the planar electrode plasma system is illustrated in figure 3.13. The electrons react faster to the RF field than the heavier positively charged ions, and are absorbed on the electrodes. Because the cathode is capacitively coupled to the ground, the flow of absorbed electrons is restricted. This leads to a negative charge buildup on the cathode, with potential strength V_{DC}. The anode is directly coupled to ground, and is therefore at zero potential. The center part of the chamber forms an equipotential region at positive potential V_P. The potential V_{DC} leads to acceleration and bombardment of the positive ions on the cathode. By placing the sample on the cathode, the surface is subject to bombardment of the high-energy ions.

The physical sputtering caused by the acceleration of ions by the electric field is not the main etching mechanism in RIE. The dominant etching mechanism is the chemical etching caused by reactions of the reactive ionized species with the sample. The gases introduced to the chamber can be used to control the etching chemistry and selectivity. Oxygen gas can be used to etch organic compounds, and offer high selectivity to inorganic materials.

If the RIE is operated with inert energized ions, such as Ar^+, the etching is pure physical sputtering. This is an example of ion milling, and will be explained in the next section. If there is only reactive gas molecules and no energized ions, the etching is purely chemical. If the electrodes are replaced by an coil that inductively couples to the plasma, which is the case for a barrel etcher, the ion bombardment on the surface is negligible and the etching is chemical and isotropic.

A conductive path should be formed from the sample to the cathode in the RIE to avoid local charge build up during the etching process. This renders RIE unsuitable for etching on non-conductive samples.

3.3.6 Inductively Coupled Plasma RIE

A limitation of conventional RIE is that the etch rate is relatively low. The etching rate is dependent on the plasma density, which in turn is dependent on the RF power. By increasing the RF power the bias on the cathode increases, which leads to more energized ion bombardment and reduction in selectivity.

Inductively coupled plasma (ICP) systems have been developed where the plasma density is controlled independently of the bias on the cathode. This is done using a radio frequency power source connected to a coil at the outside of the chamber, which inductively transfers energy to the plasma. The sample stage is connected to a second RF power source, which is used to control the voltage V_{DC}. This enables the generation of high plasma densities, while maintaining low ion bombardment energies.

3.3.7 Ion Milling

Ion milling is a pure physical ion sputtering process that can be used for materials that cannot be etched by RIE. Sub-100 nm pattern transfer can be achieved, but the selectivity between mask and substrate is generally low.

The most common gas used for ion milling is argon. This is because argon is an inert gas, so it does not chemically react with the substrate. The physical reaction between Ar^+ and the sample depends on the energy of Ar^+. Surface absorption and surface damage are the dominant processes at energies less than 10 eV. At energies over 10 keV the Ar^+ can penetrate deeply into the substrate and become implanted. Ion milling occurs when the energy of the ion is in between 10 eV and 5000 eV.

Ion milling is different from the sputtering in RIE because of the way the ions are generated. In ion milling the generation of the ions is separated from the sample etching. The ion source is separated from the sputtering chamber, and consists of a thermionic cathode that emits electrons. The electrons are accelerated towards the anode. Gas molecules enters the ion source and are ionized by the electrons. This forms a plasma of positively charged ions, which are extracted from the ion source and accelerated towards the sample in the sputtering chamber. A coil focuses the ions to a beam, which is why ion milling is also called ion beam milling. To avoid charge build up on the substrate an electron gun, called the neutralizer, is placed in the main chamber. It is a hot filament that emit electrons to neutralize the positive charge from the ion beam. Because the ion beam is neutralized, IBE can be used to etch non-conductive samples.

Because Ar^+ is inert to the materials on the substrate, the etching rate only depends on the sputtering yield of the materials. Because the difference in sputter yield for different materials is relatively small, ion milling is generally a nonselective process. The low selectivity leads to fast consumption of mask material and limited etching depth.

An issue that faces ion milling is faceting, and happens because the consumption of mask material is larger at the edges than at the planar surface. Figure 3.14 show the sample and mask before milling and after milling, and illustrates how faceting effects the etched profile. Faceting can be reduced by using a thin mask layer, which requires the mask to be made out of hard materials with low sputter yield.

The compounds formed by ion milling are nonvolatile, which allows them to redeposit everywhere. Redeposition on the sample can be reduced by tilting and rotating the sample.

(a) Intial mask pattern

(b) Faceting after ion sputtering

Figure 3.14: Illustration of faceting during ion milling. (a) Substrate and mask before milling. (b) Faceted profile after ion milling due to higher sputter yield at the edges of the mask.

Chapter 4

EXPERIMENTAL

This chapter presents the experimental methods used in this work to establish chromium-carbon hard masks. The subsequent processing steps including ion beam etching is presented for completeness, although this was not performed in this work. First, an overview of the complete nanostructuring process is given. Then, process development is described. Finally, the fabrication of hard masks on thin film samples is given.

4.1 Samples

The samples used in this work are based on (111)-oriented STO substrates. The dimensions of each substrate is approximately 5×5 mm. The samples are divided in two groups: test samples (TS) and thin film samples (TFS). Test samples are used for process development and dummy samples, and the substrates are Nb-doped to make them conductive. Thin film samples have thin films of $BaTiO_3$ and $La_{0.7}Sr_{0.3}MnO_3$ deposited by pulsed laser deposition on non-conductive STO substrates[1].

Five thin film samples are used in this work. The structure of the five TFS can be seen in figure 4.1. The structure of the TFS are chosen for investigating possible strain coupling between the ferromagnetic LSMO and ferroelectric BTO. The sample in (a) consist of a 10 nm layer of LSMO on top of STO. Sample (b) and (c) have a 10 nm and 3 nm layer of BTO grown on top of the LSMO, while for sample (d) and (e) the order of the LSMO and BTO layers are reversed, and with BTO thickness 10 nm and 3 nm respectively.

4.2 Overview of Nanostructuring Process

In this section an overview of the nanostructuring process is presented. The work flow with steps (a) to (k) for establishing freestanding nanoscale features using EBL and IBE on thin film samples can be seen in figure 4.2, and the steps involved are:

(a) The process starts out with a STO substrate with a thin film of BTO and/or LSMO

[1] Thin film growth was not part of this thesis and was carried out by Torstein Bolstad

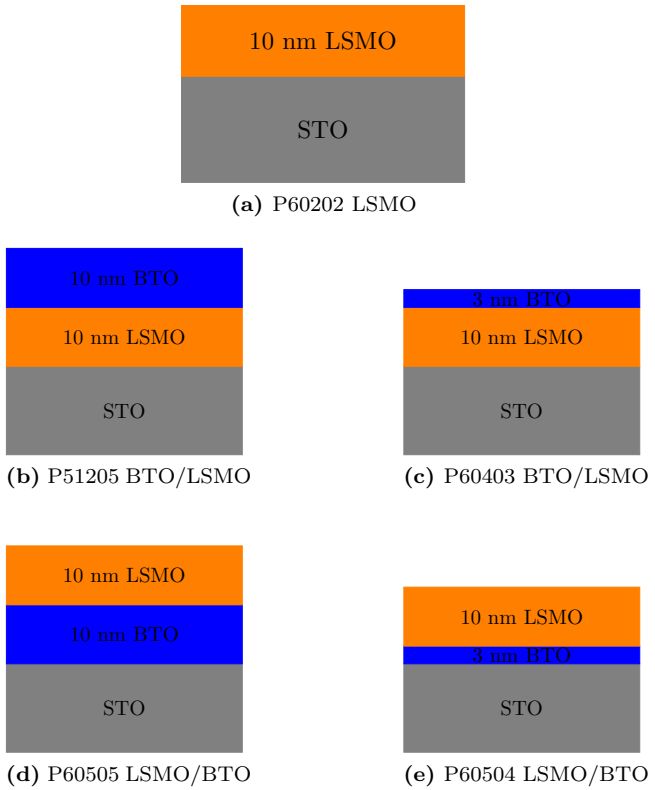

(a) P60202 LSMO

(b) P51205 BTO/LSMO

(c) P60403 BTO/LSMO

(d) P60505 LSMO/BTO

(e) P60504 LSMO/BTO

Figure 4.1: Illustration of the sample structure that were prepared with a hard mask. The samples will be used in future measurements to investigate possible coupling between the ferromagnetic and ferroelectric layers. The first structure (a) consist of a 10 nm layer of LSMO grown on top of (111)-oriented STO. The structure in (b) and (c) have a 10 nm and 3 nm layer of BTO on top, respectively. For the LSMO/BTO heterostructures in (d) and (e) the LSMO thin film has been grown on top of a 10 nm and 3 nm layer of BTO.

(b) A thin layer of carbon is evaporated in a carbon coater to form the basis for a hard mask

(c) Electron sensitive resist is spin coated and soft baked to form a uniform film

(d) The resist is selectively exposed by electron beam lithography

(e) The exposed resist is removed in a developer solution

(f) Residues of resist are removed from the exposed area in a short O_2 plasma descum

(g) A chromium thin film is deposited by electron beam evaporation

(h) The resist is removed with acetone in a lift off step, leaving behind only the chromium directly deposited on the carbon surface

(i) The chromium film is used as a hard mask during O_2 reactive ion etching of the carbon layer, resulting in a chromium-carbon hard mask

(j) Ion beam etching with argon is used to selectively remove the part of the thin film not covered by the hard mask

(k) Remaining carbon from the hard mask is removed in an O_2 inductively coupled plasma reactive ion etch

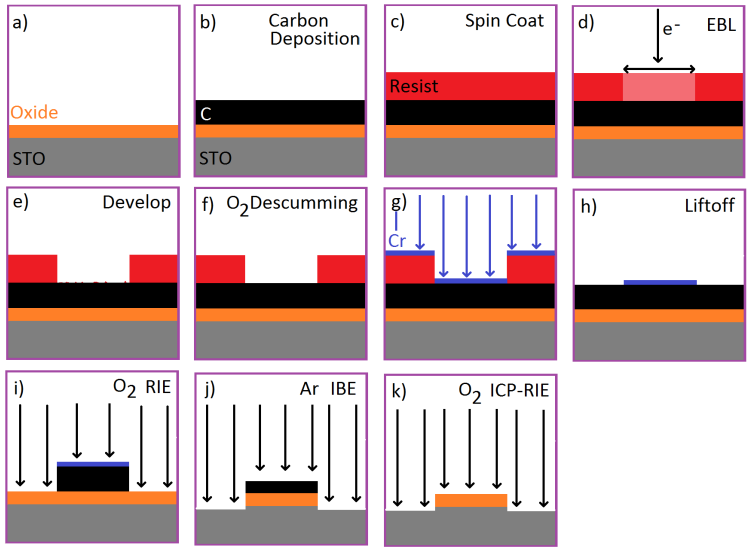

Figure 4.2: Overview of the nanostructuring recipe used to create freestanding devices from oxid thinfilms. (b) First a thinfilm of carbon is deposited in a caron coater. In steps (c) through (h) electron beam lithography is used to do lift off with chromium. (i) The pattern of the chromium is transferred to the carbon using oxygen RIE to form a chromium-carbon hard mask. (j) Argon bombardment in an ion beam etcher removes oxide not protected by the hard mask. (k) The remaining carbon mask is removed in a high-density oxygen plasma. Adopted from [49].

After establishing freestanding structures, contacts are to be deposited using lift off and connected to the measurement system with a wire bonder.

An overview of the instruments used are given in table 4.1.

Table 4.1: Instruments used for processing and characterization. NanoLab Tool ID is included as a reference for future work.

Tool name	Manufacturer and Model	NanoLab Tool ID
Carbon Coater	Cressington 208c High Vacuum Carbon Coater	1510
EBL	Elionix ELS-G100	1150
Plasma Cleaner	Diener Electronics Femto	1450
E-beam Evaporator	Pfeiffer Vacuum Classic 500	1205
ICP-RIE	Oxford Instruments Plasmalab System 100	1207
CAIBE	Oxford Instruments Ionfab 300 Plus (LC)	1240
SEM	Hitachi S-5500 S(T)EM	1512
Profilometer	Veeco Dektak 150	1720

4.3 Process Development

Process development was performed on Nb:STO substrates[2] to find the optimal parameters for establishing the chromium hard mask.

4.3.1 Method

As explained in the nanostructuring section, many of the parameters in the EBL process are interdependent. This is why a dose test is usually performed when establishing an EBL process. In this work several parameters in the EBL process are tested. For each of the parameters tested, a dose test has been performed simultaneously.

4.3.2 Resist

The objective of the resist test is to investigate if a difference in line width and edge roughness after chromium lift off can be observed by changing the resist structure from single layer to bilayer. Sample A is prepared with a single layer of PMMA, while sample B is prepared with a bilayer of PMMA and MMA. The pattern exposed in the EBL are 200 nm wide lines. After lift off the lines are imaged in the SEM.

4.3.3 Cross-section Imaging

This test is used to characterize the cross-section of the bilayer resist. This can be used to determine if there is an undercut in the bilayer resist. After developing,

[2] All test samples have a Nb:STO substrate, except for sample B which is Si.

sample B is scribed perpendicular to the lines. One of the pieces is imaged using the cross-section holder of the SEM. The stage is rotated by 30° to give an sideways view of the cross-section. The first image in the SEM is taken at 5 kV acceleration voltage, 15 µA emission current and 200k magnification. Then, the stage is rotated so that the cross-section area is perpendicular to the beam axis. The second image is taken with the emission current reduced to 0.7 µA and magnification 110k.

4.3.4 Proximity Effect Correction

BEAMER is used to perform PEC on the mask in figure 4.3, referred to as mask A. Mask A consist of a 200 nm line connected to eight 120 × 120 µm squares in a hallbar structure. The accuracy of the PEC is determined based on the clearing dose of the various areas of the mask. If the dose correction is accurate, all areas should be completely developed simultaneously.

The PEC is based on line edge dose correction with point spread function for 200 nm PMMA on Si at 100 keV electron energy. For BEAMER flow chart and standard settings see appendix A.

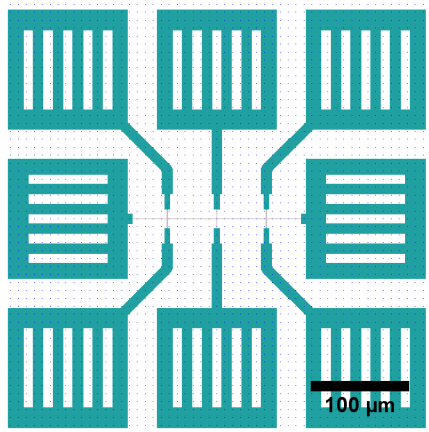

Figure 4.3: Mask A used for test samples with a center 200 nm hallbar structure and eight 120 × 120 µm^2 contact pads. The mask was designed in CleWin4.

Sample C is used for the PEC test. After developing the sample is imaged in an optical microscope to determine the clearing dose of the large features. After lift off the 200 nm line is imaged in the SEM. The dose that gives a continuous chromium pattern is selected as the clearing dose.

4.3.5 Developer Time IPA:DI 9:1

The goal of this test is to determine the dependence of line width and clearing dose on developer time and exposure dose. The result will be used to select the developer time to use in further work.

Sample C-F are used for this test. SEM images are taken of the center part of the 200 nm hall bars at all the tested exposure doses and developer times.

4.3.6 Beam Current

The beam current test is used to determine the effect of beam current on the line width and clearing dose. This will be used to determine what beam current should be used in further work.

Sample C and G are used in this test. SEM images are taken of the center part of the 200 nm hall bars at all the tested exposure doses and beam currents.

4.3.7 Developer Solution

The effect of developer solution on the line width and clearing dose is investigated. The result will be used to determine if MIBK:IPA 1:3 or IPA:DI 9:1 should be used as developer.

Sample G and H is used in this test. SEM images are taken of the center part of the 200 nm hall bars for all combinations of developer solution and exposure doses.

4.3.8 Developer Time MIBK:IPA 1:3

The goal of this test is to determine the dependence of line width and clearing dose on developer time in MIBK:IPA 1:3 and exposure dose. The result will be used to determine what is the optimal developer time for MIBK:IPA 1:3.

Sample I and H are used for this test. SEM images are taken of the center part of the 200 nm hall bars at all the tested exposure doses and developer times.

4.3.9 E-beam Evaporation Broadening

The objective of this test is to determine if there is any broadening of features during the e-beam evaporation step. This is done by imaging the resist in the SEM before lift off, and compare to the line width after lift off. Depending on the result from this test it will be known if optimization of the e-beam evaporation step is needed.

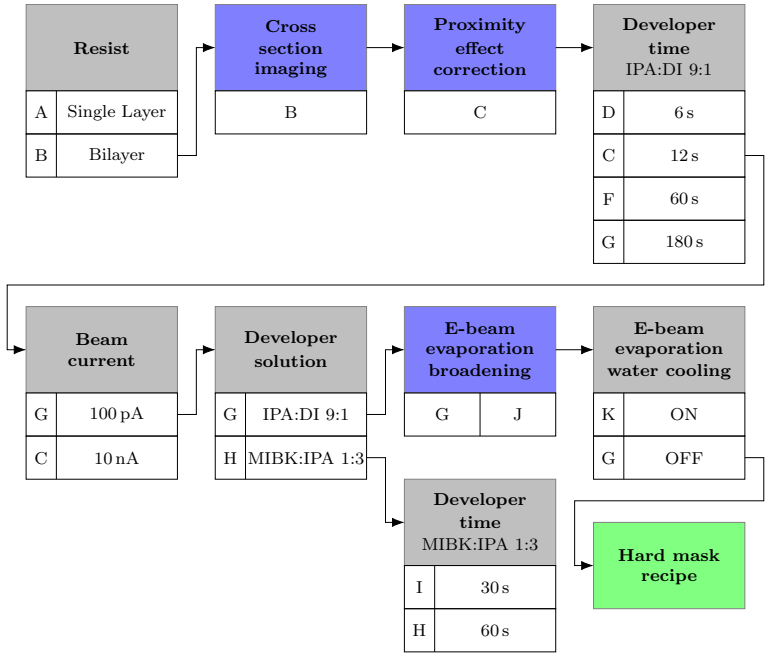

Figure 4.4: Flow chart of process development. Sample name and variable value listed in white box

Data is collected from sample G and J. Sample J is imaged in the SEM before and after lift off, and sample G is imaged only after lift off.

4.3.10 E-beam Evaporation Water Cooling

The e-beam evaporator has an option to use water cooling. This is done by bringing a cooling element in contact with the back side of the sample holder. If water cooling has an effect on line width after lift off is investigated.

Sample K is prepared with water cooling on, and sample G has water cooling off. SEM images are taken of both samples at the center part of the 200 nm hall bars.

4.3.11 Test Sample Overview

An overview of the process flow is given in figure 4.4, where the tests are presented in the order they were performed. The test samples are summarized in table 4.2.

Table 4.2: List of samples A-K used for process development. All test samples have a Nb:STO substrates, except for B which is Si.

Test	A	B	C	D	E	F	G	H	I	J	K
Resist											
Bilayer cross-section											
Proximity effect correction											
Developer time DI:IPA											
Beam current											
Developer solution											
Developer time MIBK:IPA											
E-beam evap. broadening											
E-beam evap. water cooling											
Dose											

4.3.12 Sample Preparation

This section presents the steps and variables involved in preparing sample A-K. Parameters that are varied are given in table 4.3.

Clean and Dehydrate

In the first step the samples are cleaned and dehydrated following the procedure in table 4.4. The samples are placed in acetone and ultrasonicaly agitated for 5 min. To avoid residues from contaminants in the acetone the samples are rinsed in DI water and then dried with N_2. Excess moisture is evaporated in a dehydration step on a hot plate at 180 °C for 5 min.

Spin Coating and Soft Bake

The spin coating and soft bake recipe for the single layer and bilayer resists are given in table 4.5 and 4.6, respectively.

The smallest spin coater chuck available in NanoLab is for 10×10 mm samples. Smaller samples will not cover the vacuum exhaust, and fall off as soon as the chuck starts rotating. This is an issue with the oxide samples used in this work, since they are only 5×5 mm. To solve this issue a blue low tack tape with a needle hole in it is used to protect the chuck and to avoid having resist being sucked into the spin coater motor.

After the sample is placed on the spin coater chuck and good vacuum is verified (lower than 0.8 mbar), resist is applied using a pipette. A small amount of resist is used since most will be thrown off during rotation. New pipettes are used for every sample to avoid contaminating the resist bottles. The spin coating recipes

Table 4.3: Process parameters for samples. A-K are test samples used during process development. The test samples TS1 and TS2, and thin film samples (TFS) P60202 to P60504 are used for hard mask fabrication.

Sample	Substrate	Resist	Mask	PEC	Dose [µC cm^{-2}]	Beam Current [nA]	Developer Solution	Developer Time [s]	Water Cooling
A	Nb:STO	Single	200 µm lines	No	500-1400	1.0	MIBK:IPA 1:3	30	Off
B	Si	Bilayer	200 µm lines	No	1000-3250	10	MIBK:IPA 1:3	25	Off
C	Nb:STO	Bilayer	Mask A	Yes	150-1000	10	IPA:DI 9:1	12	Off
D	Nb:STO	Bilayer	Mask A	Yes	150-1000	10	IPA:DI 9:1	6	Off
E	Nb:STO	Bilayer	Mask A	Yes	150-1000	10	IPA:DI 9:1	60	Off
F	Nb:STO	Bilayer	Mask A	Yes	150-1000	10	IPA:DI 9:1	180	Off
G	Nb:STO	Bilayer	Mask A	Yes	400-1150	0.1 and 10	IPA:DI 9:1	12	Off
H	Nb:STO	Bilayer	Mask A	Yes	300-1000	0.1 and 10	MIBK:IPA 1:3	60	Off
I	Nb:STO	Bilayer	Mask A	Yes	300-1000	0.1 and 10	MIBK:IPA 1:3	30	Off
J	Nb:STO	Bilayer	Mask A	Yes	400-1150	0.1 and 10	IPA:DI 9:1	12	Off
K	Nb:STO	Bilayer	Mask A	Yes	300-1050	0.1 and 10	IPA:DI 9:1	12	On
TS1	Nb:STO	Bilayer	Mask B	Yes	750	0.1 and 10	IPA:DI 9:1	12	Off
TS2	Nb:STO	Bilayer	Mask B	Yes	750	0.1 and 10	IPA:DI 9:1	12	Off
P60202	LSMO/STO	Bilayer	Mask B	Yes	750	0.1 and 10	IPA:DI 9:1	12	Off
P51205	BTO/LSMO/STO	Bilayer	Mask B	Yes	750	0.1 and 10	IPA:DI 9:1	12	Off
P60403	BTO/LSMO/STO	Bilayer	Mask B	Yes	750	0.1 and 10	IPA:DI 9:1	12	Off
P60505	LSMO/BTO/STO	Bilayer	Mask B	Yes	750	0.1 and 10	IPA:DI 9:1	12	Off
P60504	LSMO/BTO/STO	Bilayer	Mask B	Yes	750	0.1 and 10	IPA:DI 9:1	12	Off

Table 4.4: Cleaning and dehydration procedure

Step	Parameter
Clean	Acetone ultrasonic bath 5 min
Rinse	DI water and dry with N_2
Dehydration	Hot plate 180 °C for 5 min

Table 4.5: Recipe for spin coating and soft baking single layer resist

Step	Parameter
Resist	950k PMMA A2
First step	500 RPM for 10 s with 500 RPM/s acceleration
Second step	2000 RPM for 45 s with 500 RPM/s acceleration
Soft bake	Hot plate 180 °C for 5 min

have a first step of rotating at 500 RPM for 10 s to ensure that the resist spreads out on the sample.

After spin coating the samples are soft baked on a hot plate at 180 °C[3] for 5 min.

After soft bake the resist is inspected in an optical microscope to verify that there are no pin holes. The thickness of the resist is determined using a reflectometer with settings for PMMA resist and STO substrate.

Exposure

The resist coated samples are exposed in the EBL using the parameters in table 4.7. A constant acceleration voltage of 100 kV and write field size of $500 \times 500\ \mu m^2$. The spot sizes of the beam at different beam currents are given in table 4.8.

[3]The left hot plate on the SU-8 spin coater bench have been used for all samples. The set temperature is 155 °C, which according to the calibration is 180 °C.

Table 4.6: Recipe for spin coating and soft baking bilayer resist

Step	Parameter and value
Resist	MMA EL6
First step	500 RPM for 5 s with 200 RPM/s acceleration
Second step	8000 RPM for 60 s with 500 RPM/s acceleration
Soft bake	Hot plate 180 °C for 5 min
Resist	950k PMMA A2
First step	500 RPM for 10 s with 500 RPM/s acceleration
Second step	3000 RPM for 45 s with 500 RPM/s acceleration
Soft bake	Hot plate 180 °C for 5 min

Table 4.7: General settings for EBL

Parameter	Value
Acceleration Voltage	100 kV
Beam Current	Varies by sample, 0.1 to 10 nA
Exposure Dose	Varies by sample, 150 to 3250 µC cm^{-2}
Write field size	500×500 µm^2
Dots per write field	50000 at ≥ 1 nA
	500000 at 0.1 nA

Table 4.8: Spot size in the EBL at different beam currents

Beam current [nA]	Spot size [nm]
0.1	1.8
1.0	2.3
10	10

Some exposures are done with two beam currents. For those exposure the small features are written at 0.1 nA and the large features at 10 nA. When changing beam current a wait time of 30 min is used to let the beam current stabilize.

Develop

Developing is done by submerging the sample in a beaker with developer and gently stirring. The developers used in this work are MIBK:IPA 1:3 and IPA:DI 9:1. See table 4.2 for details on each sample. MIBK:IPA 1:3 is from MicroChem. IPA:DI 9:1 is mixed in the lab before use.

As developer stop for MIBK:IPA 1:3 the sample is submerged in IPA for 10 s and dried with N_2. For the samples developed in IPA:DI 9:1 the developing process is stopped by submerging in DI water for 30 s and dried with N_2.

Descum

Before metallization the samples are briefly descummed in the plasma cleaner to remove residual resist and promote adhesion. Parameters are given in table 4.9.

Metallization

Metallization with chromium is done in the e-beam evaporator. The parameters are given in table 4.10. The beam current is adjusted to establish an evaporation rate of 5 Å s^{-1} before the shutter is opened. Evaporation continues until the mass thickness monitor reads 20 nm, at which the shutter is closed.

Table 4.9: Recipe for descumming in plasma cleaner

Parameter	Value
Gas	Oxygen
Flow	50 %
Power	50 %
Time	12 s

Table 4.10: Parameters for metallization with chromium in e-beam evaporator.

Parameter	Value
Pressure	10^{-6}mbar or lower
Acceleration voltage	8 kV
Beam current	35-50 mA
Metal	Chromium
Thickness	20 nm
Rate	5 Å s^{-1}

Lift off

Lift off is done with acetone as the solvent. The process is divided in two parts. Most of the resist is removed in the first step. The sample is held with a tweezer at a slight angle and submerged in acetone. A squeeze bottle is used to apply a steady stream of acetone. Then, the sample is placed in a clean beaker with acetone and ultrasonically agitated for 3 min at room temperature (19 °C). Finally the sample is cleaned in DI water and dried with N_2.

4.4 Hard Mask Fabrication

In this section the fabrication of hard masks on two test sample (TS) and five thin film samples (TFS) is presented.

4.4.1 Hallbar Mask

The EBL mask used to define the hallbar structures can be seen in figure 4.5a, and is referred to as mask B. Each hallbar device occupies an area of $750 \times 750\,\mu m^2$ and consist of eight $200 \times 200\,\mu m^2$ contact pads connected to a hallbar structure in the center. The six vertical lines that connect the hallbar to the top and bottom contacts are 500 nm wide and spaced with a pitch of 20 µm.

The layout of the test samples and thin film samples are illustrated in figure 4.5c and 4.5d. The squares with a number represent one hallbar device, and the

number is the width of the hallbar in µm. The three crosses show the position of the alignment marks.

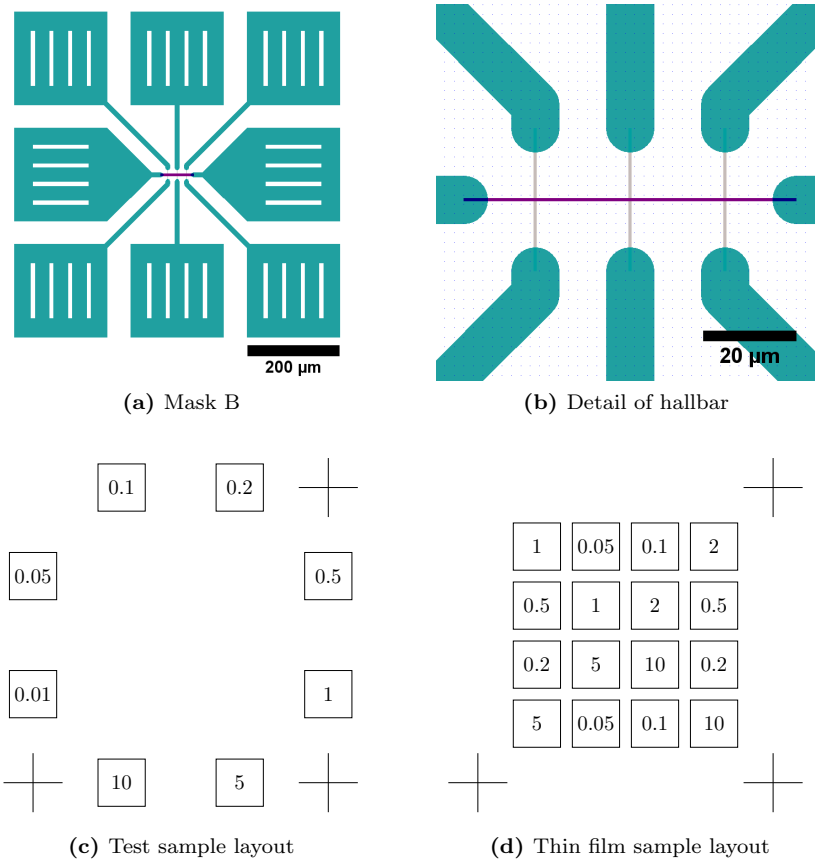

(a) Mask B

(b) Detail of hallbar

(c) Test sample layout

(d) Thin film sample layout

Figure 4.5: (a) Shows the hallbar mask (Mask B) used for fabricating the hard mask. The length of the hallbar is 60 µm. (b) shows a schematic of the layout on the sample. Each square is one instance of the hallbar device, and the number show the width of the hallbar in micrometer. The three crosses are alignment marks.

The full mask is processed in BEAMER using line edge dose correction with point spread function for 200 nm PMMA on Si at 100 keV electron energy. For BEAMER flow chart and settings see appendix A.

4.4.2 Alignment Mark

Three alignment marks are deposited on each sample using lift off according to the EBL and lift off method in section 4.3.12. Parameters for EBL and developing are

listed in table 4.11. Metallization is done in the e-beam evaporator with 10 nm of Ti and 40 nm Pt at a rate of 5 Å s^{-1}.

Table 4.11: EBL and developing parameters for alignment mark exposure

Parameter	Value
V_{acc}	100 kV
I_{beam}	10 nA
Dose	800 µC cm^{-2}
Developer	IPA:DI 9:1 for 12 s
Rinse	DI water for 30 s and dry with N_2

4.4.3 Carbon Deposition

Before carbon deposition the samples are dehydrated on a hotplate at 180 °C for 5 min. The test samples and the thin film samples are carbon coated separately. The settings are listed in table 4.12. The samples are placed on a clean Si wafer. After deposition and removal of the samples, the carbon thickness is measured on the Si wafer using the profilometer.

Table 4.12: Carbon coater parameters for test samples and thin film samples

Sample	Bias [V]	Pulse length [s]	Pulses
Test samples	4.5	6	2×5
Thin film samples	4.5	6	20

4.4.4 Chromium Hard Mask

The chromium hard mask is deposited using lift off according to the EBL and lift off method described in section 4.3.12 and parameters in table 4.3. This includes using bilayer resist for lift off and 100 pA EBL beam current for writing the hallbar and 10 nA for writing the contacts. The exposure dose is 750 µC cm^{-2}. Developing is done in IPA:DI 9:1 for 12 s. The test sample is prepared with the layout in figure 4.1c and thin film samples with the layout in figure 4.1d. After lift off the thickness of the chromium mask is measured in the profilometer.

4.4.5 Carbon Etching

Carbon etching is done in the ICP-RIE using oxygen gas. The ICP-power is turned off, so the instrument is operating as a RIE. Parameters for the test samples and the thin films samples are given in table 4.13.

Between each of the etching steps the thickness of the hard mask is measured in the profilometer.

The dimension of the hard mask is measured using the SEM and ImageJ. First, SEM images are captured for each of the hallbar devices. Then, the line width is measured using ImageJ. The line widths at three positions are collected for each picture. One of the TS is imaged in the SEM after the final RIE etching step, while TFS P60202 is imaged after the first 11 min etching step.

Table 4.13: Reactive ion etching parameters for the test samples (TS) and thin film samples (TFS).

Parameter	TS	TFS
Oxygen flow	40 sccm	40 sccm
Pressure	10 mbar	10 mbar
Temperature	20 °C	20 °C
ICP power	0	0
RF power and time	25 W 8 min	25 W 11 min
	25 W 4 min	25 W 8 min

Chapter 5

RESULTS AND DISCUSSION

This chapter presents the results from the experimental work. In the first part the results from the sample preparation is presented and discussed, starting with process optimization and followed with the characterization of the hard masks for the thin film samples. Finally, limitations with the process and suggestion for further work are discussed.

5.1 Process Development

Here the results from process development is presented following the process flow in figure 4.4. At the end of the chapter the suggested recipe and suggestions for further optimization are given.

5.1.1 Resist

In this section the results from the testing of lift off with single layer and bilayer resist is presented.

SEM images of the chromium lines 1500 $\mu C\,cm^{-2}$ can be seen in figure 5.1.

The results from the reflectometer measurements of the resist thickness is given in table 5.1. The single layer PMMA has a thickness of 100 nm. For the bilayer sample a thickness of 170 nm was measured for the bottom MMA layer and 70 nm for the top layer (numbers are rounded to the nearest 10 nm).

Table 5.1: Thickness of single layer and bilayer resist measured with reflectometer, rounded to the closest 10 nm.

Resist	Thickness [nm]
Single layer PMMA	100
Bilayer only MMA	170
Bilayer PMMA/MMA	240

Discussion

The chromium lines deposited on the single layer resist have rough features at the edges of the lines (Figure 5.1a,c,e). For the lines deposited with the bilayer resist

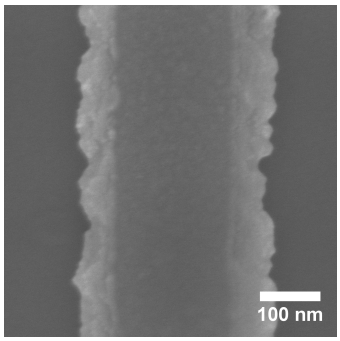

(a) Single Layer 1000 µC cm^{-2}

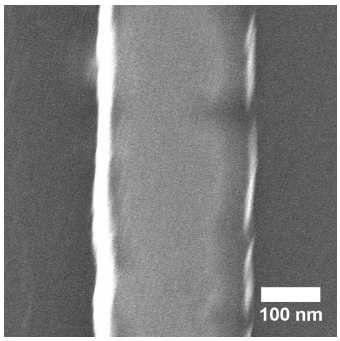

(b) Bilayer 1000 µC cm^{-2}

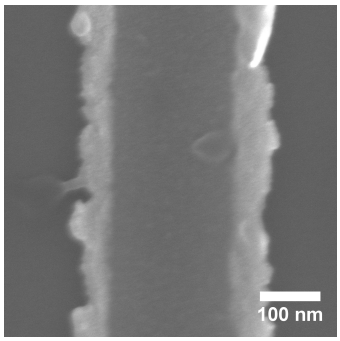

(c) Single Layer 1200 µC cm^{-2}

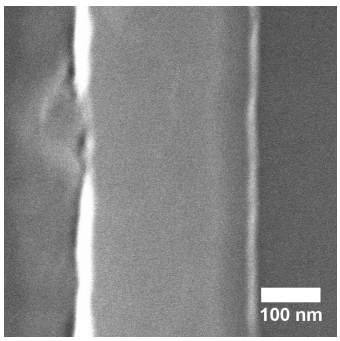

(d) Bilayer 1250 µC cm^{-2}

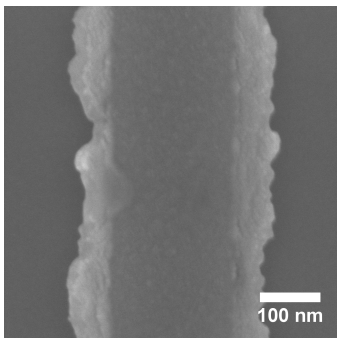

(e) Single Layer 1400 µC cm^{-2}

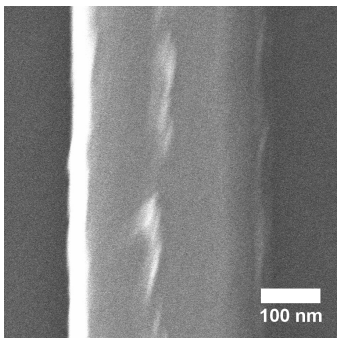

(f) Bilayer 1500 µC cm^{-2}

Figure 5.1: Comparison of chromium line after lift off for (a,c,e) single layer and (b,d,f) bilayer resist at doses between 1000 to 1500 µC cm^{-2}.

the roughness is mostly removed (5.1b,d,f). This shows that with regard to edge roughness the bilayer resist performs better than the single layer resist.

The main reason for using a bilayer resist is to get an undercut profile such as

the one described in figure 3.11. At 100 keV electron energy the sidewalls are almost vertical. This is undesirable when performing lift off, since some material will deposit on the side walls and form a continuous film. The edge roughness is possibly material from the sidewalls that remain after the lift off step.

Another reason that the bilayer performed better in this experiment is that the thickness of the single layer resist is 100 nm and the bilayer resist is 240 nm. For a more direct comparison the bilayer should have the same thickness as the single layer resist. This requires a different MMA solution. MMA EL6 is the thinnest MMA solution available in the NTNU NanoLab, and the spin coater was used at the maximum rotation speed of 8000 RPM.

Conclusion

SEM images reveal that the bilayer resist produces sharper lines with less edge roughness.

5.1.2 Cross-section Imaging

The results from the cross-section imaging of the bilayer resist on sample C is presented here. Figure 5.2a show the first SEM image of the resist profile. While enhancing the magnification and adjusting the focus, it was observed that the profile of the resist started changing. Figure 5.2b show the resist profile taken at 110k magnification and 0.7 µA emission current.

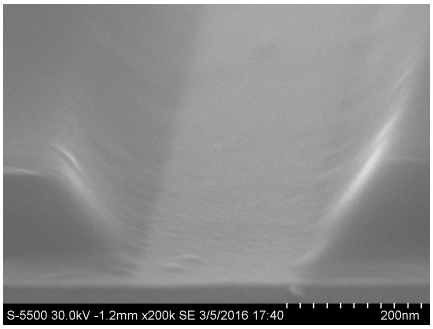

(a) Cross-section 200k magnification and 15 µA SEM emission current

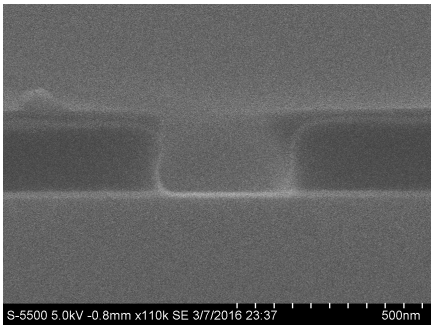

(b) Cross-section at 110k magnification and 0.7 µA SEM emission current

Figure 5.2: Cross-section images of the bilayer resist profile on sample B. (a) Taken at high magnification and long imaging time and (b) at low magnification and short imaging time.

Discussion

The change in profile on the first image is attributed to melting of the PMMA resist. At high magnification the electron beam is focused to scanning over a small area. This results in the resist being exposed, thereby reducing the PMMA polymer length and the T_g. The exposure is combined with local heating from the energetic electrons. The two effects with lower T_g and local heating explains the melting effect that is observed.

Because the second image is at a lower magnification and beam current the resist is less exposed and the heating effect is spread over a larger area. The sidewalls are more vertical than in the first image, and a slight undercut is observed.

Conclusion

The cross-section of a bilayer resist on a Si substrate has been investigated in a SEM. A slight undercut is observed in the bilayer resist. Imaging was challenging due to the interaction between the electron beam and the resist, which caused the profile of the resist to change with time.

5.1.3 Proximity Effect Correction

Here the results from the proximity effect correction is presented. The first part covers the proximity corrected mask, and is followed with experimental results.

Proximity Effect Corrected Mask

The mask after proximity effect correction can be seen in figure 5.3. The lowest dose coefficients are observed in the center area of the contact pads, ranging from 0.9 and up to 1.0, and increasing towards 1.2 at the corners. The center part of the hallbar has a dose coefficient of 1.4, which is expected since the features are small and relatively far away from the other exposed areas. For the parts of the hallbar that is closer to the contacts a stronger proximity effect is expected, which explains why the dose coefficient is lower than on the other parts of the hallbar.

Clearing dose on sample

The optical images of the sample after developing can be seen in figure 5.4 with dose increasing from $150\,\mu C\,cm^{-2}$ in the lower left corner to $1000\,\mu C\,cm^{-2}$ in the top right corner. The circumferences of the contacts are completely developed at an exposure dose of $500\,\mu C\,cm^{-2}$, while the $10\,\mu m$ lines in the contact pads are completely developed at $600\,\mu C\,cm^{-2}$.

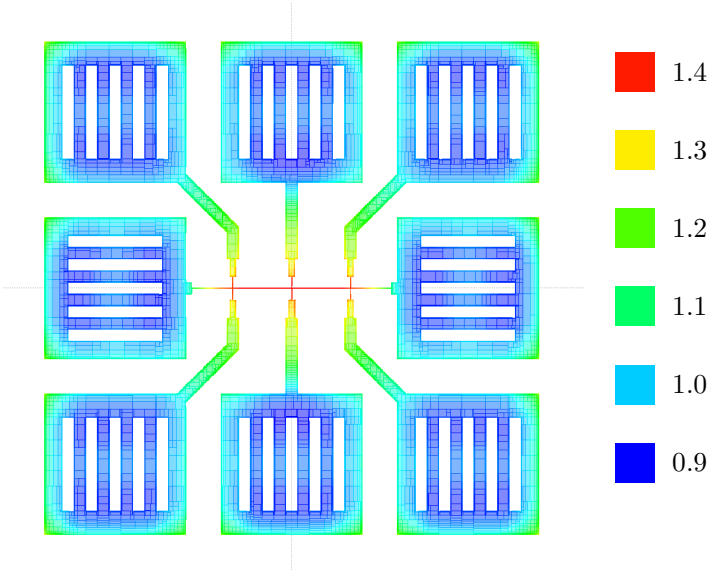

Figure 5.3: Hallbar mask from figure 4.3 after proximity effect correction in BEAMER. The colors indicate the dose coefficient following the scale on the right side.

Table 5.2: Clearing dose for circumference and 10 µm line on contact pad and 200 nm line on the hallbar using PEC mask.

Geometry	Clearing Dose [$\mu C\,cm^{-2}$]
Contact, circumference	500
Contact, 10 µm line	600
Hallbar, 200 nm line	600

SEM images of the 200 nm hallbar at 600, 650 and 700 $\mu C\,cm^{-2}$ can be seen in figure 5.5. Below 600 $\mu C\,cm^{-2}$ no continuous lines were observed, indicating that the clearing dose was not reached. The roughness of the line edges appears to be smoother at higher doses, but at the expense of increased line width. The clearing doses for the various geometries are summarized in table 5.2.

Discussion

The clearing dose varies with the feature size, hence the PEC is slightly inaccurate. Large features are cleared at lower doses than smaller and more isolated features. This indicates that the magnitude of the proximity effect is underestimated. The point spread function (PSF) used is based on electron scattering on an Si substrate, while the substrate material in the sample is STO. Table 5.3 lists the densities of Si, GaAs and STO. The higher density of STO, as compared to Si, is consistent

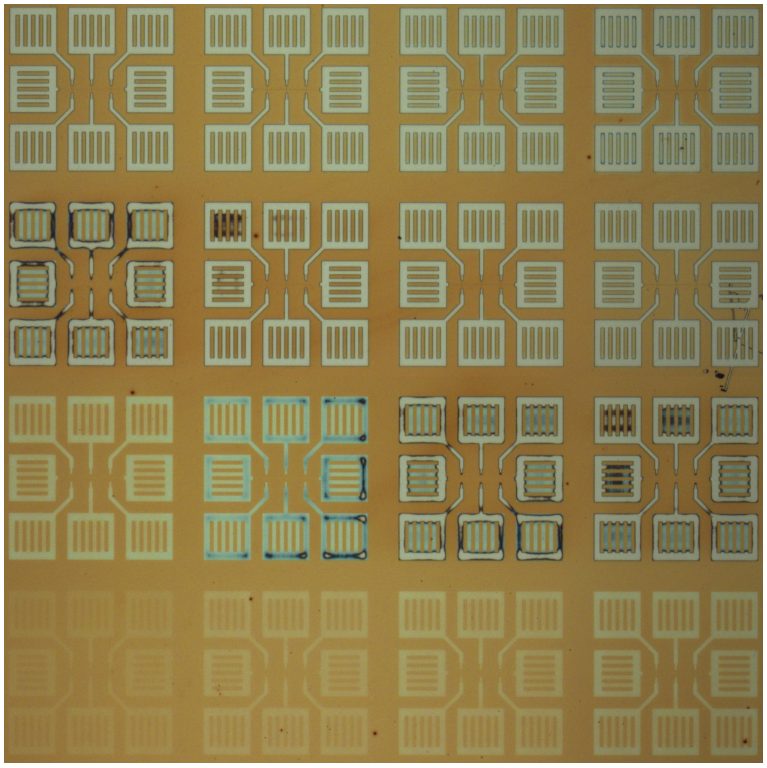

Figure 5.4: Optical image of hallbar pattern in bilayer resist after developing using PEC mask. Exposure dose starts at 150 µC cm^{-2} in the lower left corner and increases to 1000 µC cm^{-2} in the top right corner.

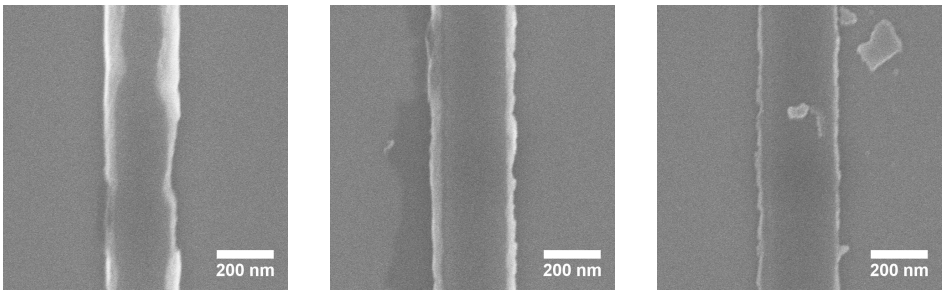

(a) 600 µC cm^{-2} **(b)** 650 µC cm^{-2} **(c)** 700 µC cm^{-2}

Figure 5.5: SEM images of the chromium lines after lift off. The lowest dose with continious adhesion of 200 nm lines of chroium is 600 µC cm^{-2}. At higher exposure doses the edges of the lines become smoother, but at the expense of increased line width.

Table 5.3: Densities of Si, GaAs and STO.

Material	Density [g cm^{-3}]	Source
Si	2.33	[108]
GaAs	5.31	[109]
STO	4.81	[110]

with increased proximity effect. The difference in density of STO and GaAs is only 10 %, which suggests that the PSF for GaAs is more accurate for STO than Si. However, PEC using the PSF for GaAs is not tested in this work due to limited time.

Conclusion

In this section proximity effect corrections were tested using a hallbar mask with various geometries. It was found that PEC based on PSF for Si substrate and 200 nm PMMA resist is a good first approach to PEC, but in the future simulations on GaAs substrate should be tested.

5.1.4 Developer Time IPA:DI 9:1

Here the results from the dose and developer time test with IPA:DI 9:1 on sample C-F is presented. For each developer time, the line width after lift off as a function of exposure dose is plotted in figure 5.6.

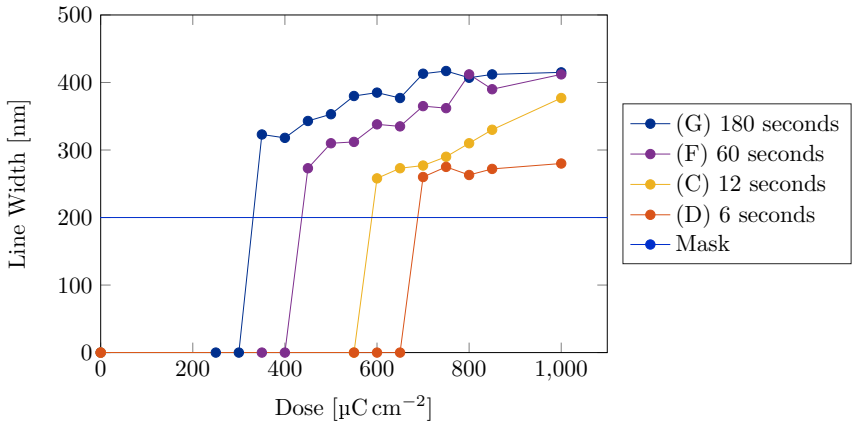

Figure 5.6: Linewidth of chromium lines following lift off in acetone at exposure doses from 150 to 1000 µC cm^{-2} and developer times of 6, 12, 60 and 180 s. The horizontal blue line illustrates the mask line width of 200 nm.

Discussion

The data in figure 5.6 can be described by the following observations. First, reducing the developer time increases the clearing dose. To dissolve the same amount of resist in a shorter amount of time, the developer rate must increase. This is achieved here by increasing the exposure dose.

The second observation is that the line width increases with developer time and exposure dose. The proximity effect is expected to give line width broadening, but the magnitude observed here with up to doubling in the line width indicate that other effects are in play. One effect that can explain the broadening is charging, since this causes the beam to defocus and deflect. Charging can be reduced by increasing the conductivity of the sample, or more simply by reducing the beam current.

Shorter developer time results in the curves that follow the mask most closely. This suggest using the shortest developer time of 6 s. On the other hand, short developer times have draw backs with respect to the manufacturing method. Developing is done manually using a stop watch. This results in small variations in developer time between each sample. The relative variations will be smaller for samples that are developed longer. Therefore, a developer time of 12 s will be used.

5.1.5 Beam Current

Here the results from the dose and beam current test on sample C (10 nA) and G (100 pA) is presented. The line width after lift off as a function of exposure dose is plotted in figure 5.7 for the two samples.

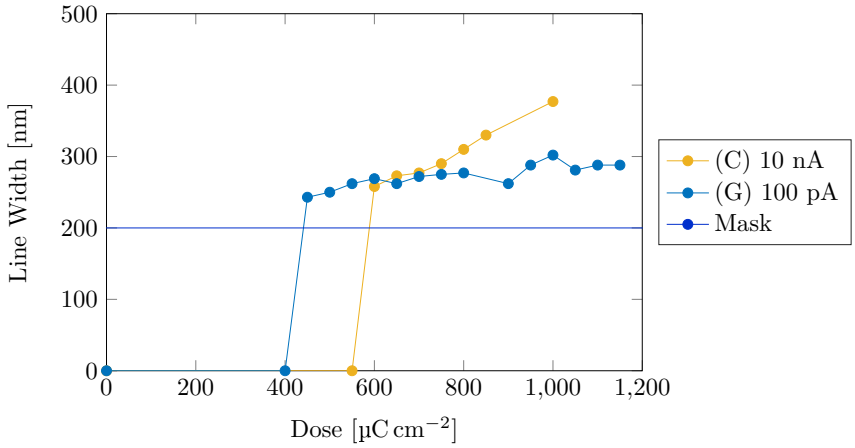

Figure 5.7: Dependence of line width on dose at 10 nA and 0.1 nA EBL beam current. Horizontal blue line illustrates the mask width of 200 nm.

Discussion

Two changes are observed when the beam current is reduced from 10 nA to 100 pA. First, the clearing dose is reduced from 600 to 450 $\mu C\,cm^{-2}$. Secondly, the line width is less sensitive towards change in exposure dose. These observations support the hypothesis that charging is an issue when writing 200 nm lines at 10 nA.

Conclusion

Based on an observed reduction in clearing dose when the beam current is decreased, it is concluded that charging is an issue when exposing at 10 nA. For future fabrication a beam current of 100 pA should be used on critical areas of the pattern where high accuracy is needed.

5.1.6 Developer Solution

Here the results from the dose and developer solution test on sample G (IPA:DI 9:1 12 s) and H (MIBK:IPA 1:3 60 s) is presented. Figure 5.8 show the line width as a function of exposure dose for the two developer solutions.

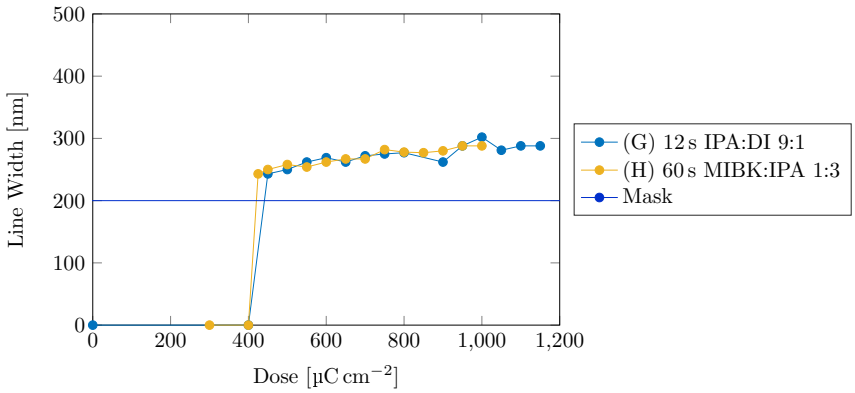

Figure 5.8: Comparison of MIBK:IPA 1:3 and IPA:DI 9:1 as developers with regard to line width. Horizontal blue line illustrates the mask width of 200 nm.

Discussion

No significant change in line width is observed when changing from IPA:DI 9:1 for 12 s to MIBK:IPA 1:3 for 60 s. In section 5.1.4 a decrease in line width was observed when the developer time is reduced, which suggests that developing for a shorter time in MIBK:IPA 1:3 might give a line width closer to that of the mask.

Conclusion

Developing in MIBK:IPA 1:3 for 60 s does not have an observable benefit over IPA:DI 9:1 for 12 s as developer with respect to produced line widths. MIBK:IPA 1:3 has a larger room for reducing developer time, which might reduce line width.

5.1.7 Developer Time MIBK:IPA 1:3

Here the results from varying the MIBK:IPA 1:3 developer time on sample H (60 s) and I (30 s) is presented. Figure 5.9 show the line width as a function of exposure dose for the two developer times.

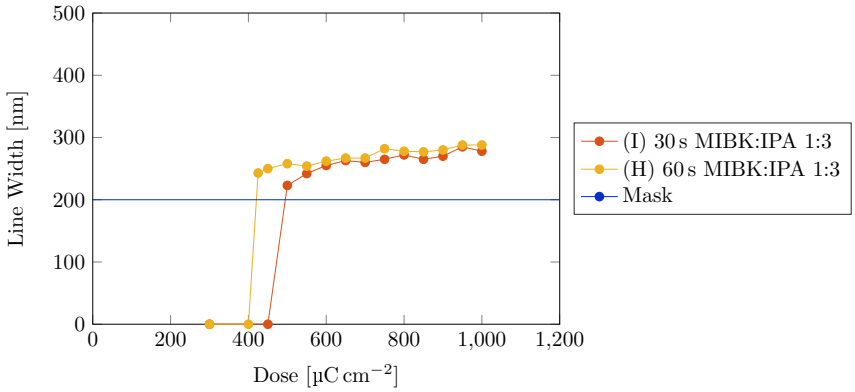

Figure 5.9: Dependence of line width as a function of dose with MIBK:IPA 1:3 as developer at 30 and 60 s developer time. Horizontal blue line illustrates the mask width of 200 nm.

Discussion

The data in figure 5.9 can be described with the following observations: First, reducing the developer time from 60 s to 30 s increases the clearing dose from 425 µC cm^{-2} to 500 µC cm^{-2}. This is the same trend as was observed with IPA:DI 9:1 as developer. Secondly, line width increases slightly with developer time and exposure dose. This is explained by the proximity effect. The change in line width is much smaller than what was observed for IPA:DI 9:1 in figure 5.8. This attributed to less charging effects for the MIBK:IPA 1:3 samples, since they were written at lower beam current than the IPA:DI 9:1 samples.

No significant benefit is observed for using MIBK:IPA 1:3 as developer instead of IPA:DI 9:1. On the contrary, IPA:DI 9:1 can be mixed from IPA and DI water before every use, which has a practical benefit with respect to no limitations on shelf life. Because of this, IPA:DI 9:1 will be used as the developer in further work.

Conclusion

Decreasing the developer time in MIBK:IPA 1:3 from 60 s to 30 s result in an increase in clearing dose from 425 µC cm^{-2} to 500 µC cm^{-2}. The line width is not substantially reduced, indicating that the contrast in exposure dose is sharp. No significant improvements with using MIBK:IPA 1:3 is observed, which is why IPA:DI 9:1 will be used in further work.

5.1.8 E-beam Evaporation Broadening

Here the results from the dose test on J is presented. The first part covers the results from investigating resist melting in the SEM. Then, the measurement of line width before and after lift off is given.

Figure 5.10 show and SEM image of the resist after developing. Before imaging the width of the lines was the same across the whole image. However, before the image was captured, the features close to the center started expanding.

The line widths of in the resist after developing, as well as after lifting off, as a function of exposure dose can be seen in figure 5.11.

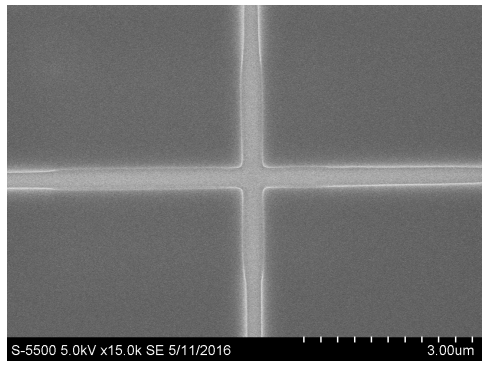

Figure 5.10: Melting of resist observed in the SEM. Initially, the line width was the same across the whole sample. Before the image was captured, the features in the center broadened, as is seen by the curved lines.

Discussion

The change in dimensions observed when capturing the SEM image in figure 5.10 can be explained by resist melting. Similar melting was observed on the cross-section sample in section 5.1.2.

Because of the broadening effect, the exact line width in the resist cannot be determined in the SEM. Still, the line width measured in the SEM can be used

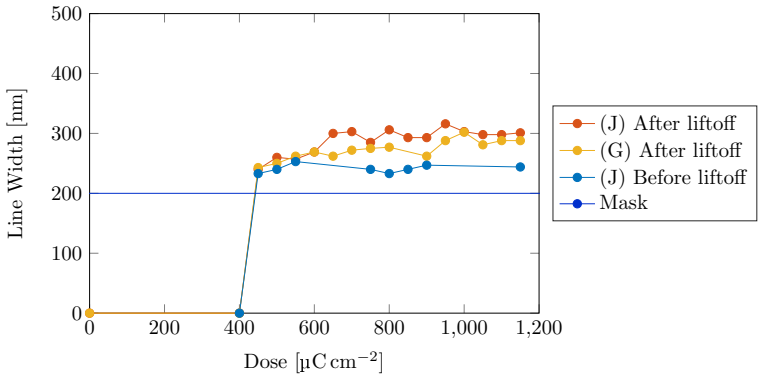

Figure 5.11: Line width before and after lift off for sample J and after lift off for sample G.

as an upper bound. If the e-beam evaporation process has no intrinsic broadening effect, the line width measured on sample J before lift off should be the same, or smaller, than after lift off.

The plot in figure 5.11 show that the line width after developing is fairly insensitive to exposure dose, while the line width after lift off is larger and sensitive to exposure dose.

The results for sample G is included in the plot since it was not inside the SEM before lift off. This way, the effect of imaging the resist in the SEM can be eliminated by comparing sample J after developing with sample G after lift off. The discrepacy between sample G and J after lift off is thus attributed to effects from imaging the resist in the SEM.

From figure 5.11 it is clear that the e-beam evaporation process contributes to giving a line width larger than that of the mask. One possibility to why this happens is electron or UV radiation from the e-beam source[111]. It is also possible that the radiant heat from the source heats the resist above the glass transition temperature T_g, which for PMMA is usually between 95 and 106 °C[112].

Conclusion

SEM imaging of the developed resist was challenging due to the resist melting upon exposure to the electron beam, resulting in broadening in the features. The line width in the resist is smaller than the line width in the metal lines after lift off, and the difference increases with exposure dose. This suggests that heating or exposure of the resist during e-beam evaporation is a problem.

5.1.9 E-beam Evaporation Water Cooling

Here the results from the dose and water cooling test on sample G and K is presented. The resulting line widths after lift off as a function of exposure dose can be seen in figure 5.12.

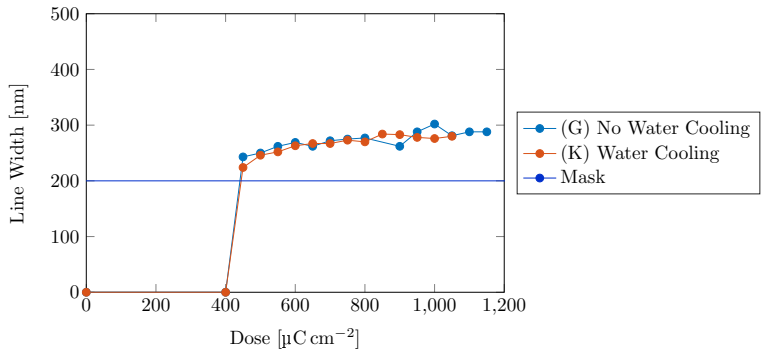

Figure 5.12: Linewidth after lift off for sample G and K. Water cooling was used during e-beam evaporation for sample K, while no active cooling was used on sample G.

Discussion

No real change in line width is observed for the water cooled sample. This indicates either that heating is not an issue in the process, or that the heat transport from the sample to the cooling block was insufficient.

The sample is separated from the Al cooling block with an intermediate Si wafer. If the Al cooling block and the Si wafer are not perfectly flat, there will be small pockets of vacuum between them that restricts the flow of heat. This can be solved by applying some sort of vacuum safe heat conducting oil, or by removing the Si wafer and placing the sample directly on the Al cooling block.

If heating is not the issue, the broadening effect during e-beam evaporation may come from exposure to electrons.

Conclusion

No real change was observed for the sample prepared using water cooling during e-beam evaporation of chromium. The result from the water cooling test is inconclusive, as the intermediate Si wafer is believed to disrupt the flow of heat. More testing with water cooling should be done in the future.

5.2 Hard Mask Fabrication

In this section the results from characterization of the hard mask structuring process is presented. First, profilometer data from the test sample is used to determine the thickness and roughness of the deposited and etched films. Then, the SEM images of the hard mask on the test sample and one thin film sample is presented.

5.2.1 Profilometer Data

Profilometer data from the test sample after carbon deposition, chromium lift off and RIE etching can be seen in figure 5.13.

The profilometer data for the carbon deposition (Fig 5.13a) reveal that the carbon film has a mean thickness of 52 nm. The variation in thickness is $\sigma = 11$ nm. During deposition of carbon, sparks were observed from the carbon source. The chromium profile in figure 5.13b reveal a step height of 22 nm with variations within 5 nm. The profile of the hard mask after RIE etching show a step height of 73 nm with variations captured within 3 nm.

Discussion

The variation in thickness of the carbon film may not be an issue when writing structures that are larger than 100 nm, but will be an issue if nanoscale devices are to be realized. When establishing nanoscale devices, the thickness of the carbon mask should be thick enough to avoid implantation and damage from the argon ions to the oxide. At the same time, the thickness should be as small as possible to avoid high aspect ratios in the hard mask, which may lead to loading effects and faceting during the sputtering step.

Furthermore, the carbon film in figure 5.13b show a spike in thickness at position 600 µm that is about 90 nm taller than the other parts of the carbon film. No spike is seen on the reference part of the sample, where no carbon was deposited. This indicates that the spike results from the carbon deposition process. The sparks that were observed during evaporation can explain the occurrence of the spikes, since this will result in small patches of carbon deposition at random positions.

From previous work [49] the sputter selectivity of the carbon mask to BTO and STO was found to be about 1:1. A selectivity of 1:3 has been observed when the carbon is deposited by e-beam evaporation[113]. The low selectivity of this carbon film is explained by the difference in vacuum in the carbon coater ($> 10^{-4}$mbar) and an e-beam evaporator ($< 10^{-6}$mbar). Without a very high vacuum, oxygen present in the chamber will react with the carbon and reduce the sputter resistance[47].

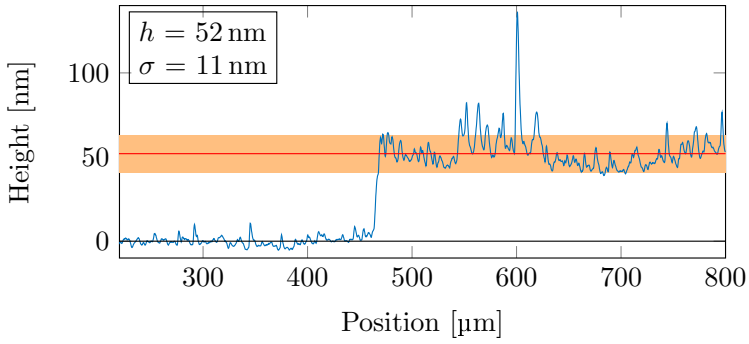

(a) Carbon profile

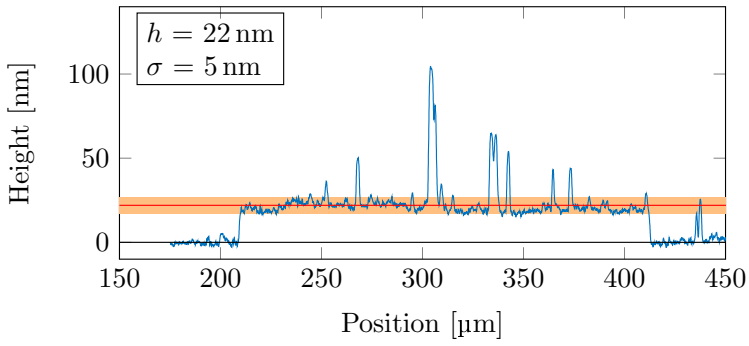

(b) Chromium profile

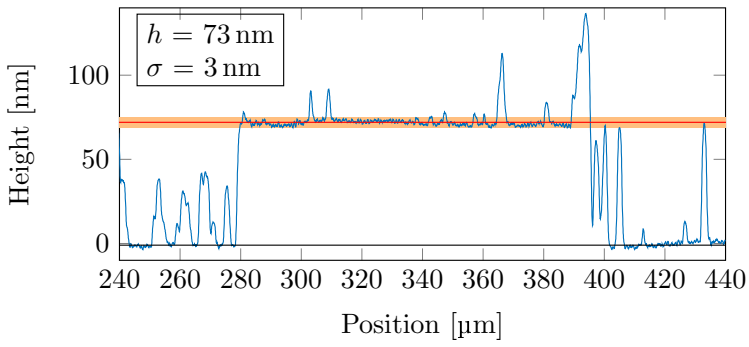

(c) Hard mask profile

Figure 5.13: Profilometer data of (a) carbon deposition, (b) chromium lift off and (c) RIE etching. Step height h is the height of the red line. Orange area encapsulate flucuations in profile, exluding outliers, and is used to determine variation in step height σ.

Because of the above issues with non-uniformity and poor selectivity, deposition

of carbon with the carbon coater is not ideal. If available, e-beam evaporation should be used to deposit carbon. This was the original plan in this project, but carbon was not allowed in the e-beam evaporator at NanoLab because it would contaminate the chamber and the samples of other users.

The chromium film in figure 5.13b has a spike similar to the one observed on the carbon film. The variations in the profile of the chromium film are explained by the roughness of the underlying carbon film. The variations are smaller than what was measured on the carbon film, which is attributed to the ultrasonic clean before deposition of chromium. A peak is observed at position 430 nm that has the same thickness as the chromium mask. This can be a residue from the lift off process, and will mask the underlying carbon during RIE etching, resulting in additional features in the hard mask.

The profile of the hard mask in figure 5.13c has a relatively uniform thickness along the center, with the exception some peaks that are explained by variation in the carbon film. On the outside of the box some spikes with the same height as the hard mask are observed. This is explained by the chromium residues from the lift off process. The additional features are not an issue if they are not in direct contact with the hall bar, since they will not affect the transport properties. However, the goal of this project is to establish a process that can be used for any geometries, and then it is critical that no residues are left after the lift off process. The residues can possibly be removed by using an acetone spray gun and longer time in the ultrasonic bath.

Conclusion

Profilometer data reveal that the carbon film has poor uniformity that will limit the possibility of establishing sub-100 nm devices. Combined with poor sputter selectivity, this makes the carbon film deposited in the carbon coater non-ideal for this application. If available, an e-beam evaporator should be employed for depositing the carbon film at high vacuum. The lift off process leaves residues of chromium that mask areas of the sample that is supposed to be covered. The chromium residues may be an issue when writing patterns other than the hallbar.

5.2.2 Etch Rate

The step heights before and after RIE etching on the test sample (TS) and thin film sample (TFS) are listed in table 5.4. For the test sample the thickness of the chromium hard mask h_0 is measured to 20 nm. After etching for 8 min the carbon layer is completely etched through, since no further etching is observed in the second 4 min etching step. Because the time the carbon film was completely etch through the exact etch rate cannot be determined. A minimum value can be

estimated by assuming that it took the whole etching time, 8 min, to get through. This gives a minimum carbon etch rate of 6 nm min^{-1}.

Table 5.4: Step heigth before and after RIE etching on test sample (TS) and thin film sample (TFS). t_i is the etching time before measuring h_i.

Sample	h_0 [nm]	t_1 [min]	h_1 [nm]	t_2 [min]	h_2 [nm]
TS	20 ± 1	8	73 ± 1	12	73 ± 1
TFS	15 ± 1	11	73 ± 2	19	88 ± 3

The thickness of the chromium layer in the TFS is 15 nm. After etching for 11 min the step height is increased to 73 nm, and after another 8 min the step height is 88 nm. This gives an etch rate of carbon of 5 nm min^{-1}.

Discussion

The carbon etch rate in the thin film sample is smaller than the etch rate on the test sample. The two samples were etched on different days. Even though the chamber was conditioned before each run, the etch rates are as much as 20 % different. Etching for a longer time then necessary may not be an issue in this process, since the oxygen plasma will not etch the chromium mask or the oxide substrate. For future samples, the etching process can start with a short etch to determine the etch rate at that time, and then calculate how long the total time should be based on the total thickness of the carbon layer.

Conclusion

The etch rate of carbon in the RIE is found to be 5-6 nm min^{-1}. The etch rate was observed to vary from day to day. Because of the variations, a calibration run should be done before etching any samples in the RIE.

5.2.3 Pattern Transfer

Figure 5.14a show the SEM image of a hallbar hard mask after RIE etching. The image is taken at 32° tilt. Figure 5.14b show a detail of the mask at greater magnification.

The line widths of the hard mask at the various hallbar widths are listed in table 5.5.

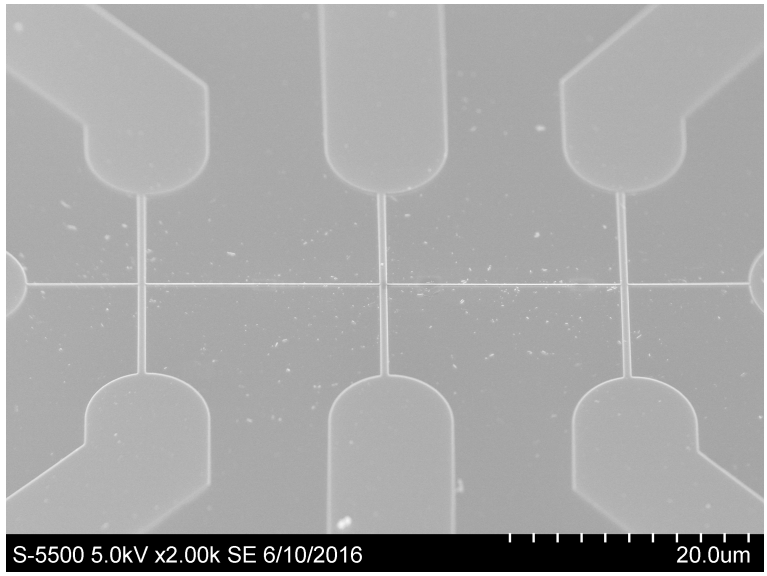

(a) Hallbar Device

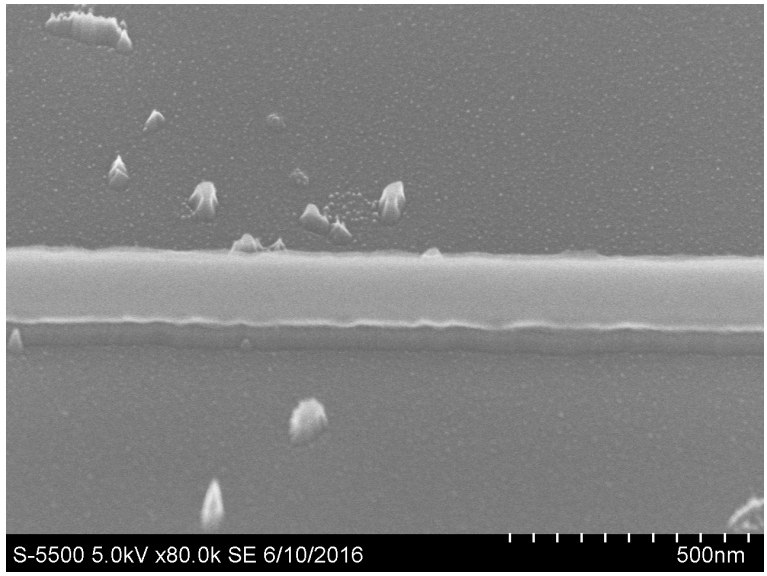

(b) Detail

Figure 5.14: Hard mask after RIE etching of carbon on TFS P60202. Image (a) show an overview of the hallbar device, with the probes from the contact pads extending from the ouside of the image. (b) Show a detail of the hallbar device, revealing edge roughness and apperance of unintended structures ouside the mask.

Table 5.5: Line width of hard mask on test sample and thin film sample

EBL mask width [µm]	Hard mask width [µm]	
	TS	TFS
10	10.9 ± 0.1	10.9 ± 0.1
5	5.4 ± 0.1	5.4 ± 0.1
2	-	2.2 ± 0.1
1	1.16 ± 0.01	1.15 ± 0.01
0.5	0.62 ± 0.01	0.63 ± 0.01
0.2	0.32 ± 0.01	0.30 ± 0.01
0.1	0.21 ± 0.01	0.20 ± 0.01
0.05	0.14 ± 0.01	0.13 ± 0.01

Discussion

Figure 5.14a reveal that the hard mask replicates the EBL mask. No discontinuities in the hard mask is observed. In agreement with the profilometer result in figure 5.13c, speckles are observed outside the hard mask pattern. Figure 5.14b shows the speckles in greater detail. Some of the speckles have the same brightness as the chromium film, which supports that chromium residues are left after lift off. Other features have the same brightness as the carbon layer, and are believed to be remains from the sparks observed during carbon evaporation.

The data in table 5.5 reveals that the width of the hard mask is greater than the EBL mask, and that the difference increases with line width. This supports that the proximity effect is strong on the oxide samples. This agrees with the observation of line width broadening during process optimization. However, the magnitude of the broadening is larger for the hard mask samples. The increase in line width for the 200 nm mask is 120 nm. For comparison, for sample G used during process development the broadening on the 200 nm line is 60 nm. The difference in process parameters for the two samples is the size of the contacts and the presence of a carbon layer in the hard mask samples. The two hard mask samples, TS and TFS, have carbon layers of different thickness, but the line width is the same. Because of changing the carbon thickness does not alter the line width, the presence of the carbon layer cannot explain the increase in broadening for the hard mask samples. This leaves the greater size of the contacts, resulting in stronger proximity effect, as the reason why the lines are significantly broader.

The broadening due to the proximity effect can be reduced by moving the contact pads further away from the hallbar and reducing the width of the probes connecting the contact pads and the hallbar. Improved PEC based on GaAs substrate, as mentioned in section 5.1.3, is also expected to reduce the broadening.

Conclusion

The SEM images reveal that the EBL pattern is reproduced in the chromium-carbon hard mask using the lift off and RIE etching techniques. Residues from the chromium lift off process act as a mask during RIE etching and leaves small unintended features outside the EBL mask. The line width of the test sample and thin film sample is the same, indicating that difference in carbon thickness has no observable effect on the line width. It is found that the large contacts on the hard mask samples result in broadening of the hallbar. To create smaller features, the contact pads should be moved further away from the hallbar and the connecting probes should be made thinner.

5.3 Suggested Recipe

Here the suggested recipe for fabricating the chromium-carbon hard mask is given. This can be used by future users as a starting point when designing a process. The parameters are listed in table 5.6-5.13. Suggested parameters for use in the IBE and ICP-RIE (step j and k) are given in table 5.14 and 5.15, and are based on the process parameters from the project work [49].

Table 5.6: Carbon coater deposition

Step	Value
Clean	Acetone ultrasonic bath 5 min
Rinse	DI water and dry with N_2
Dehydration	Hot plate 180 °C for 5 min
Carbon coater	4.5 V and 6 s pulses until desired thickness

Table 5.7: Spin coating of bilayer PMMA/MMA

Step	Value
Clean	Acetone ultrasonic bath 5 min
Rinse	DI water and dry with N_2
Dehydration	Hot plate 180 °C for 5 min
Dispense	MMA EL6 by pipette
Spin up	500 RPM for 10 s with 200 RPM/S
Spin off	8000 RPM for 45 s with 500 RPM/S
Soft bake	Hot plate 180 °C for 5 min
Dispense	950k PMMA A2 by pipette
Spin up	500 RPM for 10 s with 500 RPM/S
Spin off	3000 RPM for 45 s with 500 RPM/S
Soft bake	Hot plate 180 °C for 5 min

Table 5.8: Electron beam lithography exposure

Parameter	Value
Acceleration voltage	100 kV
Beam current	100 pA for small features
	10 nA for large features
PEC	BEAMER, Si substrate with 200 nm PMMA film
Exposure dose	750 µC cm^{-2}
Write field size	500×500 μm^2
Dots per write field	50 000 at 10 nA beam current
	500 000 at 100 pA beam current

Table 5.9: Developer process

Step	Value
Develop	IPA:DI 9:1 for 12 s
Rinse	DI water for 30 s and dry with N_2

Table 5.10: Descum parameters in plasma cleaner

Parameter	Value
Gas	Oxygen
Flow	50 %
Power	50 %
Time	12 s

Table 5.11: Chromium deposition

Parameter	Value
Source	Chromium
Pressure	10^{-6} mbar or lower
Acceleration voltage	8 kV
Rate	5 Å s^{-1}
Thickness	20 nm on mass thickness monitor

Table 5.12: Lift off

Step	Value
Lift off	In acetone in ultrasonic bath for 3 min
	at room temperature
Clean	DI water and dry with N_2

Table 5.13: Carbon etching in RIE

Parameter	Value
Gas	Oxygen
Flow	40 sccm
Pressure	10 mbar
Temperature	20 °C
ICP power	0 W
RF power	25 W
Carbon etch rate	5-6 nm min^{-1}

Table 5.14: Ion beam etching in the CAIBE. Etch rates from December 2015 included for reference. From [49].

Parameter	Value
Source voltage	500 V
Acceleration voltage	500 V
Beam current	200 mA
Neutralizer current	240 mA
Tilt	5° off normal
Rotation	20 RPM
Argon flow 1	10 sccm
Argon flow 2	5 sccm
Pressure	10 mbar
Temperature	20 °C
BTO/STO etch rate	3.8 nm min^{-1}
Chromium etch rate	5 nm min^{-1}
Carbon etch rate	3.1 nm min^{-1}

Table 5.15: Carbon etching in ICP-RIE

Parameter	Value
Gas	Oxygen
Flow	40 sccm
Pressure	10 mbar
Temperature	20 °C
ICP power	1000 W
RF power	20 W
Time	2 min

Chapter 6

CONCLUSIONS

A patterning technique for establishing a two-layer hard mask of chromium and carbon has been developed. Lines with width down to 130 nm have been established using a bilayer lift off technique.

Patterning is done using electron beam lithography (EBL) and lift off with chromium, and the chromium pattern is transferred to the underlying carbon layer using oxygen reactive ion etching. Ion beam etching (IBE) was not done during this work due to instrument down time. In the future, IBE will be used to transfer the pattern into the oxide thin films and substrate. The IBE has an neutralizer, which removes charging from the etching process. This is important when working on non-conducting substrates.

The hard mask patterning process has been developed for a 100 keV EBL system. It was found that a bilayer of PMMA and MMA give greater control on edge roughness, as compared with only a single layer of PMMA.

The resolution and stability of the EBL process is greatly dependent on EBL beam current. Writing fine features at 10 nA beam current resulted in strong dependence of line width on exposure dose and developer time. Writing the same features at 100 pA greatly reduced the sensitivity of the process. Because of this, fine features are written using low beam current, while large features such as contact pads are written at high beam current. The line width broadening is attributed to charging effects in the substrate when writing at high beam currents.

Both IPA:DI 9:1 and MIBK:IPA 1:3 are tested as developers. No real difference is observed with respect to line width.

Line width broadening is observed during e-beam evaporation of chromium. The origin of the broadening mechanism is not determined, but is believed to originate from heat and electron radiation during evaporation.

With the current recipe, line widths are approximately 60 nm wider than the EBL mask, which is attributed to strong proximity effects in the oxide substrate. The broadening effect depends strongly on the geometry of the mask, and is stronger when the mask has features over 10 µm in size close to the hallbar.

The carbon film is found to have poor uniformity, with thickness varying by 11 nm for a 52 nm layer. Thin films have poor reproducibility, which further handicaps the carbon coater deposition method. Furthermore, the 1:1 sputter selectivity of the carbon layer observed in previous work is not solved. If this recipe is to be

used successfully, evaporation of carbon should be done at higher vacuum in an e-beam evaporator.

To achieve further reduction in line width and establish the smallest possible structures, the bilayer resist should be made thinner. In the current work, the thickness is 240 nm. The chromium hard mask is about 20 nm thick, which suggest a resist thickness of 60-100 nm should work well.

Five thin film samples of $BaTiO_3$ and $La_{0.7}Sr_{0.3}MnO_3$ on (111)-oriented $SrTiO_3$ substrates have been prepared with a hard mask. The hard mask consist of hallbar devices with widths from 11 µm and down to 130 nm. The composition of the hard mask is 73 nm carbon, capped by a 15 nm chromium layer.

Further Work

The process of establishing freestanding structures was not completed due to downtime on the IBE. Only a few more steps are required to complete the samples when the IBE is back up. These steps are described below.

The next step in the process is to use to the two hard mask test samples to determine the sputter rates in the IBE. The sputter rates will be used to determine the required time to etch 40 nm into the films samples, enough to establish freestanding hallbar structures.

The remaining work includes deposition of 10 nm titanium and 50 nm gold to form contact pads. Then, with a wirebonder the contacts of the hallbar are bonded to the contacts of the electronic transport measurement system.

Transport properties will be determined both at zero magnetic field, as well as at an applied magnetic field, at temperatures down to 50 K. This way the effect of nanostructuring as well as the STO phase transition at 105 K on the transport properties of LSMO can be probed.

Appendix A

PROXIMITY EFFECT CORRECTION IN BEAMER

This appendix presents the method used for PEC and mask preparation in BEAMER.

BEAMER is a software developed by GenISys for preparing data for exposure in EBL. The software offers a comprehensive set of functions, and only a few of them were tested in the limited time frame of this work. Future users can use the work here as a starting point for exploring the remaining options available in BEAMER.

Programming in BEAMER is easy as soon as the basic method is understood. The programming language requires little experience with programming, since everything is done through a visual interface.

BEAMER will be explained using the program (called flow diagram) used in this work. The flow diagram is much like an assembly line. The data file is imported at one side, transported by wires and manipulated at several nodes, before the output is exported at the other side. The flow diagram used in this work can be seen in figure A.2. The red squares are nodes and the gray lines are the wires. Each node has a specific function, and may take several inputs and outputs.

The flow diagram used in this work has one input and four outputs. Starting from the bottom left in figure A.2 are the output for the alignment marks, large features, small features and finally Au/Ti contact pads.

In GDSII Imports the mask from a .gds file.

Extract Filters layers. Only the layers selected in the node are given as output.

Heal Combines all the layers in the input to one layer and removes overlapping features.

Merge Combines mask from several wires. The layers number is conserved, so if one input has layer 1-2 and the other has layer 2-3, layer 2 from the two inputs will be merged to the same layer, while layer 1 and 3 will remain separate.

PEC Applied proximity effect correction. The PEC used here is based on line edge dose correction. See figure A.1 for details. The same PEC is used for all masks.

Out CON Export node. Saves the input as an .CON file, which can be directly imported to the Elionix WECAS software for EBL writing.

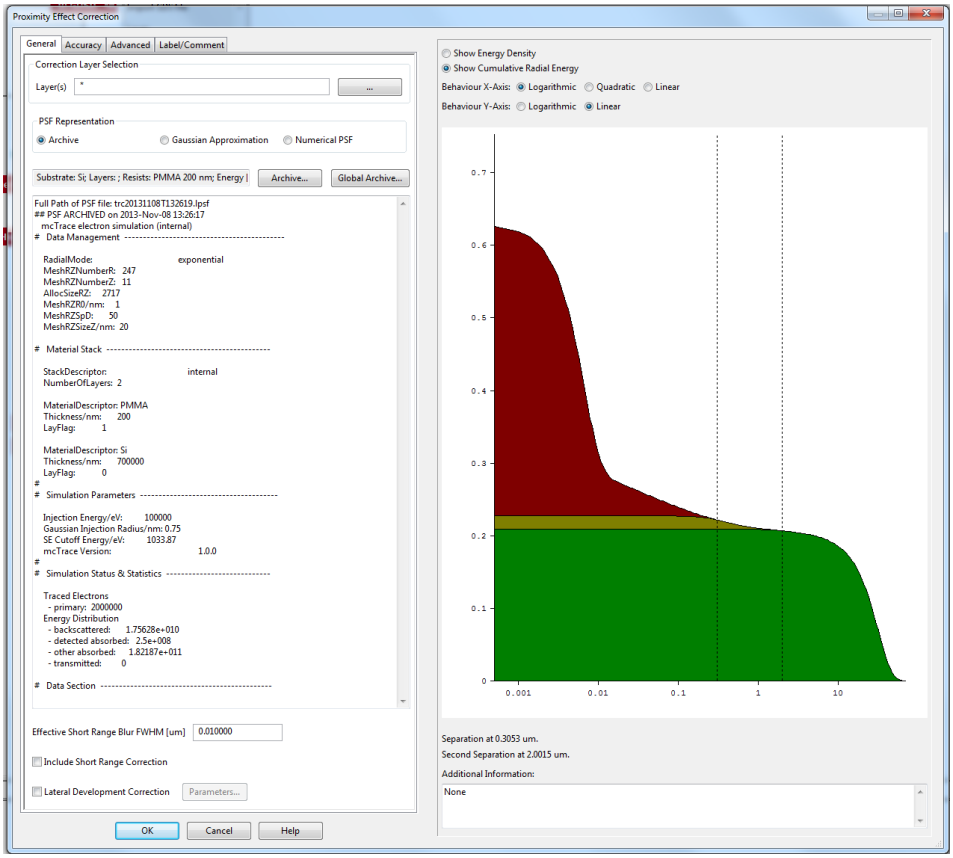

Figure A.1: Proximity effect correction settings in BEAMER. Settings are listed in the left column. The plot on the right hand side show the point spread function assuming beam FWHM is 0.01 µm.

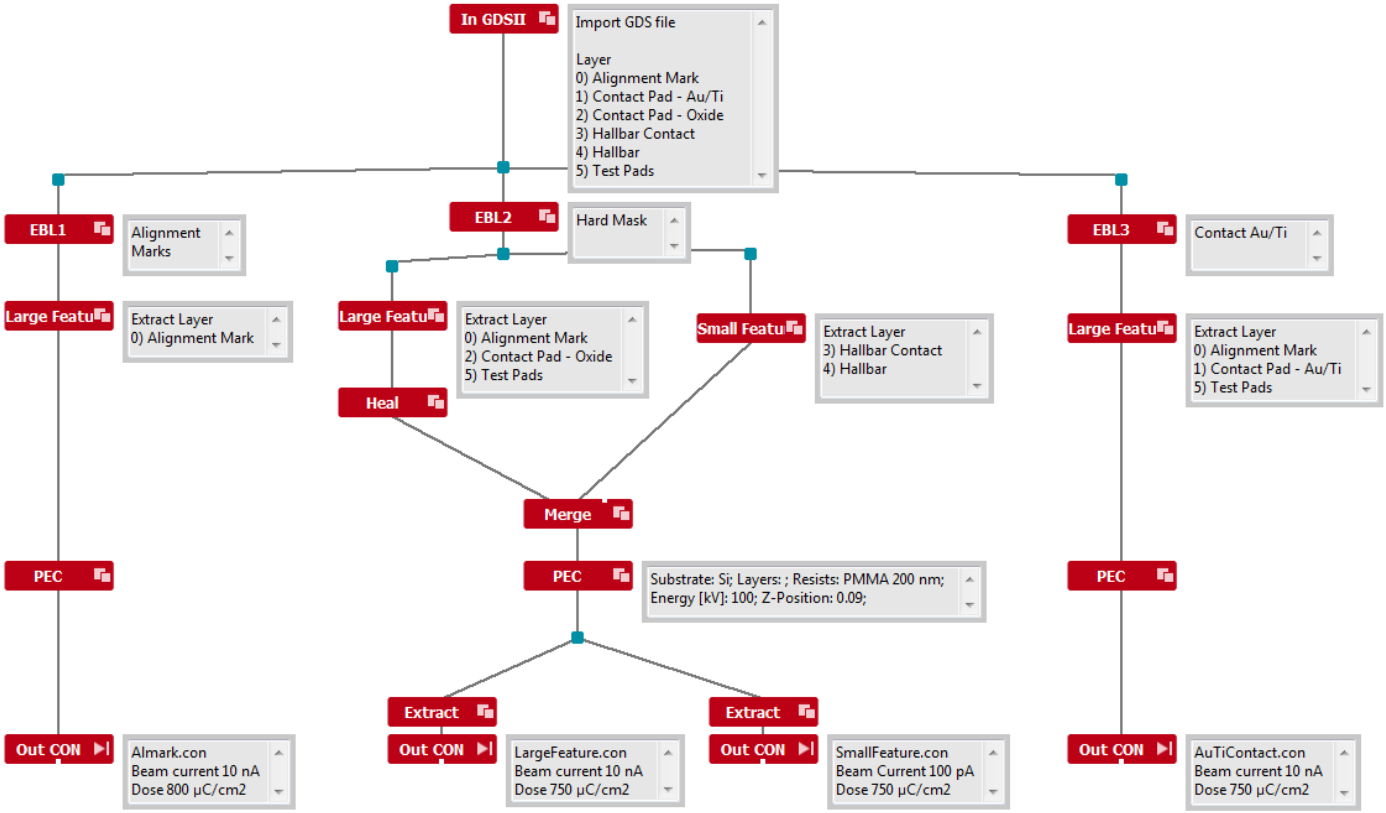

Figure A.2: BEAMER flow diagram for adding proximity effect correction. The mask GDS file is taken as input at the top and processed to create four output Elionix CON files. The EBL1 branch extracts the alignment mark layer and performs PEC on it. The EBL2 branch is used to process the hard mask pattern, and the output is saved in two CON files, one for large features that will be written at 10 nA and one for small features that will be written at 100 pA. The EBL3 branch is used to process the pattern for defining metal contacts.

REFERENCES

[1] R.D. Hicks. *De Anima*. Cambridge University Press, 1907, 405 a20–22.

[2] S. D. Bader. "Colloquium: Opportunities in nanomagnetism". In: *Rev. Mod. Phys.* 78.1 (2006), pp. 1–15.

[3] John F Gregg. "Spintronics: a growing science." In: *Nat. Mater.* 6.11 (2007), pp. 798–799.

[4] Jairo Sinova and Igor Žutić. "New moves of the spintronics tango". In: *Nat. Mater.* 11.5 (2012), pp. 368–371.

[5] Greg Szulczewski, Stefano Sanvito, and Michael Coey. "A spin of their own." In: *Nat. Mater.* 8.9 (2009), pp. 693–695.

[6] M. N. Baibich et al. "Giant magnetoresistance of (001)Fe/(001)Cr magnetic superlattices". In: *Phys. Rev. Lett.* 61.21 (1988), pp. 2472–2475.

[7] G. Binasch et al. "Enhanced magnetoresistance in layered magnetic structures with antiferromagnetic interlayer exchange". In: *Phys. Rev. B* 39.7 (1989), pp. 4828–4830.

[8] Gordon E. Moore. "Cramming more components onto integrated circuits". In: *IEEE Solid-State Circuits Newsl.* 20.3 (2006), pp. 33–35.

[9] Alberto P. Guimarães. *Principles of Nanomagnetism*. 1st ed. Vol. XXXIII. 2. Springer, 2012, p. 233.

[10] J Stohr. *MagnetismFrom Fundamentals to Nanoscale Dynamics*. Springer, 2006.

[11] B Y M Mitchell Waldrop, O F Moore S Law, and More Interesting. "More Than Will Soon Abandon Its Pursuit". In: *Nature* 530 (2016), p. 145.

[12] Wolfgang Arden et al. ""More-than-Moore" White Paper". In: (2010). URL: `http://www.itrs.net/links/2010itrs/irc-itrs-mtm-v2`.

[13] L. Berger. "Emission of spin waves by a magnetic multilayer traversed by a current". In: *Phys. Rev. B* 54.13 (1996), pp. 9353–9358.

[14] J.C. Slonczewski. "Current-driven excitation of magnetic multilayers". In: *J. Magn. Magn. Mater.* 159.1-2 (1996), pp. L1–L7.

[15] Arthur P. AP Ramirez. "Oxide electronics emerge". In: *Science (80-.).* 315.5817 (2007), pp. 1377–1378.

[16] Joerg Heber. "Materials science: Enter the oxides". In: *Nature* 459.May (2009), pp. 28–30.

[17] J Mannhart and D G Schlom. "Oxide interfaces–an opportunity for electronics." In: *Science* 327.5973 (2010), pp. 1607–1611.

[18] Martin Gajek et al. “Tunnel junctions with multiferroic barriers”. In: *Nat Mater* 6.4 (2007), pp. 296–302.

[19] C. Israel, M. J. Calderon, and N. D. Mathur. “The current spin on manganites”. In: *Mater. Today* 10.24 (2007).

[20] C. N. R. Rao and L. Gopalakrishnan. *New Directions in Solid State Chemistry*. 1997, p. 561.

[21] D Khomskii. “Spin Electronics”. In: ed. by Michael Ziese and Martin J Thornton. Berlin, Heidelberg: Springer Berlin Heidelberg, 2001. Chap. Electronic, pp. 89–116.

[22] J.G. Bednorz and K.a. Muller. “Possible High Tc Superconductivity in the Ba - La - Cu - O System”. In: *Zeitschrift für Phys. B Condens. Matter* 64 (1986), pp. 189–193.

[23] Y Tokura and Y Tomioka. “Colossal magnetoresistive manganites”. In: *J. Magn. Magn. Mater.* 200.1-3 (1999), pp. 1–23.

[24] Manuel Bibes and Agnes Barthelemy. “Oxide spintronics”. In: *IEEE Trans. Electron Devices* 54.5 (2007), pp. 1003–1023.

[25] E Vescovo et al. “Direct evidence for a half-metallic ferromagnet”. In: *Nature* 392.April (1998), pp. 794–796.

[26] Herb Kroemer. *Quasi-Electric and Quasi-Magnetic Fields in Non-Uniform Semiconductors*. 1957.

[27] A Ohtomo and H Y Hwang. “A high-mobility electron gas at the LAO/STO heterointerface.” In: *Nature* 427.6973 (2004), pp. 423–426.

[28] N. Reyren et al. “Superconducting interfaces between insulatin oxides”. In: *Science (80-.).* 317.August (2007), pp. 1196–1199.

[29] Manuel Bibes. “Towards a magnetoelectric memory Out of the scalar sand box”. In: *Nature* 7.June (2008), pp. 425–426.

[30] J P Carlo et al. “New magnetic phase diagram of (Sr,Ca)2RuO4”. In: *Nat Mater* 11.4 (2012), pp. 323–328.

[31] I. Hallsteinsen et al. “Surface stability of epitaxial La0.7Sr0.3MnO 3 thin films on (111)-oriented SrTiO3”. In: *J. Appl. Phys.* 113.18 (2013), pp. 0–6.

[32] Aldo Raeliarijaona and Huaxiang Fu. “Various evidences for the unusual polarization behaviors in epitaxially strained (111) BaTiO3”. In: *J. Appl. Phys.* 115.5 (2014), pp. 0–6.

[33] M. K. Lee et al. “Strain modification of epitaxial perovskite oxide thin films using structural transitions of ferroelectric BTO substrate”. In: *Appl. Phys. Lett.* 77.2000 (2000), p. 3547.

[34] Hong Ying Zhai et al. “Giant discrete steps in metal-insulator transition in perovskite manganite wires”. In: *Phys. Rev. Lett.* 97.16 (2006), pp. 1–4.

[35] Yoshihiko Yanagisawa et al. “Digitalized magnetoresistance observed in (La,Pr,Ca)MnO3 nanochannel structures”. In: *Appl. Phys. Lett.* 89.25 (2006).

[36] T. Z. Ward et al. “Time-Resolved Electronic Phase Transitions in Manganites”. In: *Phys. Rev. Lett.* 102.8 (2009), p. 87201. ISSN: 00319007. DOI: 10.1103/PhysRevLett.102.087201.

[37] T. Z. Ward et al. “Dynamics of a first-order electronic phase transition in manganites”. In: *Phys. Rev. B* 83.12 (2011), p. 125125.

[38] T. Z. Ward et al. “Reemergent Metal-Insulator Transitions in Manganites Exposed with Spatial Confinement”. In: *Phys. Rev. Lett.* 100.24 (2008), p. 247204.

[39] Jian-Chun Wu et al. “Study of anomalous I-V characteristics in spatially confined manganite structures”. In: *Appl. Phys. Lett.* 91.10 (2007).

[40] G. Singh-Bhalla et al. “Intrinsic tunneling in phase separated manganites”. In: *Phys. Rev. Lett.* 102.7 (2009), pp. 1–4. ISSN: 00319007. DOI: 10.1103/PhysRevLett.102.077205. arXiv: 0707.4411.

[41] T. Zhang et al. “Particle size effects on interplay between charge ordering and magnetic properties in nanosized La0.25Ca0.75MnO3”. In: *Phys. Rev. B* 76.17 (2007), p. 174415.

[42] Deliang Zhu, Hong Zhu, and Yuheng Zhang. “Hydrothermal synthesis of La0.5Ba0.5MnO3 nanowires”. In: *Appl. Phys. Lett.* 80.9 (2002), pp. 1634–1636. ISSN: 00036951. DOI: 10.1063/1.1455690.

[43] T Zhang et al. “Hydrothermal synthesis of single-crystalline La0.5Ba0.5MnO3 nanowires at low temperature”. In: *J. Mater. Chem.* 14 (2004), pp. 2787–2789.

[44] Battogtokh Jugdersuren et al. “Large low field magnetoresistance in La0.67Sr 0.33MnO3 nanowire devices”. In: *J. Appl. Phys.* 109.1 (2011), pp. 2009–2012. ISSN: 00218979. DOI: 10.1063/1.3493693.

[45] K. Shantha Shankar et al. “Fabrication of ordered array of nanowires of La0.67Ca0.33MnO3 (x=0.33) in alumina templates with enhanced ferromagnetic transition temperature”. In: *Appl. Phys. Lett.* 84.6 (2004), pp. 993–995. ISSN: 00036951. DOI: 10.1063/1.1646761.

[46] G. Singh-Bhalla, A. Biswas, and A. F. Hebard. “Tunneling magnetoresistance in phase-separated manganite nanobridges”. In: *Phys. Rev. B - Condens. Matter Mater. Phys.* 80.14 (2009), pp. 1–7.

[47] Asmund Monsen et al. “Point contact investigations of film and interface magnetoresistance of La0.7Sr0.3MnO3heterostructures on Nb:SrTiO3”. In: *J. Magn. Magn. Mater.* 374 (2015), pp. 433–439.

[48] Pier Paolo Aurino et al. “Nano-patterning of the electron gas at the LaAlO3/SrTiO3 interface using low-energy ion beam irradiation”. In: *Appl. Phys. Lett.* 102.May (2013), p. 201610. DOI: 10.1063/1.4807785.

[49] E. S. Digernes. *Nanostructuring of BaTiO3 thin films on (111)-oriented Nd-doped SrTiO3 substrates*. 2015.

[50] Ana Claúdia Lourenço Santana Marques. "Advanced Si pad detector development and SrTio3 studies by emission channeling and hyperfine interaction experiments". PhD thesis. 2009.

[51] Lizhi Liang et al. "Research progress on electronic phase separation in low-dimensional perovskite manganite nanostructures." In: *Nanoscale Res. Lett.* 9.1 (2014), p. 325.

[52] P. Schiffer et al. "Low temperature magnetoresistance and the magnetic phase diagram of La1-xCaxMnO3". In: *Phys. Rev. Lett.* 75.18 (1995), pp. 3336–3339. ISSN: 0031-9007. DOI: 10.1103/PhysRevLett.75.3336.

[53] Myron B. Salamon and Marcelo Jaime. "The physics of manganites: Structure and transport". In: *Rev. Mod. Phys.* 73.3 (2001), pp. 583–628.

[54] Elbio Dagotto. "Complexity in strongly correlated electronic systems." In: *Science* 309.5732 (2005), pp. 257–62. DOI: 10.1126/science.1107559. arXiv: 0509041 [cond-mat].

[55] L. Zhang. "Direct Observation of Percolation in a Manganite Thin Film". In: *Science (80-.).* 298.5594 (2002), pp. 805–807. ISSN: 00368075.

[56] M Uehara et al. "Percolative phase separation underlies colossal magnetoresistance in mixed-valent manganites". In: *Nature* 399.6736 (1999), pp. 560–563. ISSN: 0028-0836. URL: http://dx.doi.org/10.1038/21142.

[57] A Asamitsu et al. "Current switching of resistive states in magnetoresistive manganites". In: *Nature* 388.6637 (1997), pp. 50–52.

[58] Elbio Dagotto, Takashi Hotta, and Adriana Moreo. "Colossal magnetoresistant materials: the key role of phase separation". In: *Phys. Rep.* 344.1-3 (2001), pp. 1–153.

[59] John B. Goodenough. "Theory of the role of covalence in the perovskite-type manganites [La,M(II)]MnO3". In: *Phys. Rev.* 100.2 (1955), pp. 564–573. ISSN: 0031899X. DOI: 10.1103/PhysRev.100.564.

[60] E Dagotto and Y Tokura. "A brief introduction to strongly correlated electronic materials". eng. In: *Multifunct. Oxide Heterostruct.* Oxford: Oxford University Press, 2012.

[61] G.H. Jonker and J.H. Van Santen. "Ferromagnetic compounds of manganese with perovskite structure". In: *Physica* 16.3 (1950), pp. 337–349.

[62] S Jin et al. "Thousandfold Change in Resistivity in Magnetoresistive La-Ca-Mn-O Films". In: *Science (80-.).* 264.5157 (1994), pp. 413–415.

[63] Cengiz Şen, Gonzalo Alvarez, and Elbio Dagotto. "First order colossal magnetoresistance transitions in the two-orbital model for manganites". In: *Phys. Rev. Lett.* 105.9 (2010), pp. 1–4. ISSN: 00319007. DOI: 10.1103/PhysRevLett.105.097203.

[64] A. J. Millis, P. B. Littlewood, and B. I. Shraiman. "Double exchange alone does not explain the resistivity of La1-xSrxMnO3". In: *Phys. Rev. Lett.* 74.25 (1995), pp. 5144–5147. ISSN: 00319007. DOI: 10.1103/PhysRevLett.74.5144. arXiv: 9501034v1 [arXiv:cond-mat].

[65] A. Urushibara et al. "Insulator-metal transition and giant magnetoresistance in LSMO". In: *Phys. Rev. B* 51.20 (1995), pp. 14103–14109. ISSN: 0163-1829. DOI: 10.1103/PhysRevB.51.14103.

[66] M. Bowen et al. "Nearly total spin polarization in La2/3Sr1/3MnO3 from tunneling experiments". In: *Appl. Phys. Lett.* 82.2 (2003), pp. 233–235. ISSN: 00036951. DOI: 10.1063/1.1534619. arXiv: 0211158 [cond-mat].

[67] C.A. Randall, R.E. Newnham, and L.E. Cross. *History of the First Ferroelectric Oxide, BaTiO3*. Tech. rep. Materials Research Institute - The Pennsylvania State University, 2009.

[68] Burcu Ertuğ. "The Overview of The Electrical Properties of Barium Titanate". In: *Am. J. Eng. Res.* 2.08 (2013), pp. 1–7.

[69] H F Kay and P Vousden. "XCV. Symmetry changes in barium titanate at low temperatures and their relation to its ferroelectric properties". In: *London, Edinburgh, Dublin Philos. Mag. J. Sci.* 40.309 (1949), pp. 1019–1040.

[70] Wilma Eerenstein et al. "Multiferroic and magnetoelectric materials". In: *Nature* 442759.August (2006), pp. 759–765.

[71] Sang-Wook Cheong and Maxim Mostovoy. "Multiferroics: a magnetic twist for ferroelectricity". In: *Nat. Mater.* 6.1 (2007), pp. 13–20.

[72] G A Smolenskii and I E Chupis. "Ferroelectromagnets". In: *Physics-Uspekhi* 25.7 (1982), pp. 475–493.

[73] T Katsufuji et al. "Dielectric and magnetic anomalies and spin frustration in hexagonal RMO R Y,Yb, and Lu". In: *Phys. Rev. B* 64.10 (2001), p. 104419.

[74] Manfred Fiebig. "Revival of the magnetoelectric effect". In: *J. Phys. D. Appl. Phys.* 38.8 (2005), R123–R152.

[75] E H Hall. "On a New Action of the Magnet on Electric Currents". In: *Am. J. Math.* 2.3 (1879), pp. 287–292.

[76] R. S. Popovic. *Hall Effect Devices, Second Edition*. Series in Sensors. CRC Press, 2003, p. 448.

[77] Charles Kittel. *Introduction to Solid State Physics*. Wiley, 2004, p. 704.

[78] D K Schroder. *Semiconductor Material and Device Characterization*. Wiley, 2006.

[79] Manijeh Razeghi. *Fundamentals of Solid State Engineering*. Springer Science & Business Media, 2009, chapter 8, page 792.

[80] E H Hall. "On the "Rotational Coefficient" in Nickel and Cobalt". In: *Phil.Mag.* 12 (1881), p. 157.

[81] Naoto Nagaosa et al. “Anomalous Hall effect”. In: *Rev. Mod. Phys.* 82.2 (2010), pp. 1539–1592.

[82] E M Pugh and T W Lippert. “Hall e.m.f. and Intensity of Magnetization”. In: *Phys. Rev.* 42.5 (1932), pp. 709–713.

[83] Robert Karplus and J. M. Luttinger. “Hall effect in ferromagnetics”. In: *Phys. Rev.* 95.5 (1954), pp. 1154–1160.

[84] J Smit. “The spontaneous hall effect in ferromagnetics I”. In: *Physica* 21.6 (1955), pp. 877–887.

[85] J Smit. “The spontaneous hall effect in ferromagnetics II”. In: *Physica* 24.1 (1958), pp. 39–51.

[86] L. Berger. “Side-jump mechanism for the hall effect of ferromagnets”. In: *Phys. Rev. B* 2.11 (1970), pp. 4559–4566.

[87] A Asamitsu and Y Tokura. “Hall effect in LSMO”. In: *Phys. Rev. B* 58.1 (1998), pp. 47–50.

[88] M. Jaime et al. “Hall-Effect Sign Anomaly and Small-Polaron Conduction”. In: *Phys. Rev. Lett.* 78.5 (1997), pp. 951–954.

[89] Z Cui. *Nanofabrication: Principles, Capabilities and Limits*. Springer US, 2009.

[90] I Haller, M Hatzakis, and R Srinivasan. “High-resolution Positive Resists for Electron-beam Exposure”. In: *IBM J. Res. Dev.* 12.3 (1968), pp. 251–256.

[91] A F Mayadas and R B Laibowitz. “One-Dimensional Superconductors”. In: *Phys. Rev. Lett.* 28.3 (1972), pp. 156–158.

[92] Kenji Yamazaki and Hideo Namatsu. “5-nm-Order Electron-Beam Lithography for Nanodevice Fabrication”. In: *Jpn. J. Appl. Phys.* 43.6B (2004), pp. 3767–3771.

[93] P W Hawkes and E Kasper. *Principles of Electron Optics*. Academic Press, 1989.

[94] John Rouse, Xieqing Zhu, and Eric Munro. “Solution of electron optics problems with space charge in 2D and 3D”. In: *SPIE* 2522 (1995), pp. 375–386. ISSN: 0277786X.

[95] Bo Wu and Andrew R Neureuther. “Energy deposition and transfer in electron-beam lithography”. In: *J. Vac. Sci. Technol. B* 19.6 (2001), p. 2508.

[96] Kenji Murata, Takayuki Matsukawa, and Ryuichi Shimizu. “Monte carlo calculations on electron scattering in a solid target”. In: *Jpn. J. Appl. Phys.* 10.6 (1971), pp. 678–686.

[97] Mihir Parikh and David F. Kyser. “Energy deposition functions in electron resist films on substrates”. In: *J. Appl. Phys.* 50.2 (1979), pp. 1104–1111.

[98] Eric Munro. “Electron and ion optical design software for integrated circuit manufacturing equipment”. In: *J. Vac. Sci. Technol. B Microelectron. Nanom. Struct.* 15.June (1997), p. 2692. ISSN: 0734211X. DOI: 10.1116/1.589710.

[99] M Parikh. “Self-consistent proximity effect correction technique for resist exposure (SPECTRE)”. In: *J. Vac. Sci. Technol. B Microelectron. Nanom. Struct.* 15.3 (1977), pp. 931–933.

[100] Shazia Yasin, D Hasko G., and H Ahmed. “Comparison of MIBK/IPA and water/IPA as PMMA developers for electron beam nanolithography”. In: *Microelectron. Eng.* 61.1-3 (2002), pp. 745–753.

[101] Mark C Rosamond and Edmund H Linfield. “Contrast-sensitivity behaviour of PMMA in 7 : 3 IPA : water developer”. In: (2008), p. 3000.

[102] M Quirk and J Serda. *Semiconductor Manufacturing Technology*. Prentice Hall, 2001.

[103] Tedpella. *Carbon Coater*. URL: https://www.tedpella.com/carbon{_}html/carbon-rods-shapers.htm (visited on 05/30/2016).

[104] I. M. Watt. *The principles and practice of electron microscopy*. Cambridge University Press, 1985.

[105] M. Hatzakis, B J Canavello, and J M Shaw. “Single-step Optical Lift-off Process”. In: *Ibm J. Res. Dev.* 24.4 (1980), pp. 452–460.

[106] S. Y. Chou et al. “Sub-10 nm imprint lithography and applications”. In: *J. Vac. Sci. Technol.* 15.6 (1997), pp. 2897–2904. ISSN: 0734211X. DOI: 10.1109/DRC.1997.612486.

[107] Z Cui. *Micro-Nanofabrication Technologies and Applications*. Springer, 2006.

[108] Sigma-Aldrich. *Safety Data Sheet: Silicon*. 2016.

[109] Sigma-Aldrich. *Safety Data Sheet: Gallium Arsenide*. 2016.

[110] Sigma-Aldrich. *Safety Data Sheet: Strontium Titanate (111)*. 2016.

[111] Kezia Cheng et al. “Effects of Electron Radiation Generated during E-beam Evaporation on a Photoresist Liftoff Process”. In: *2010 CS MANTECH Conf.* 781 (2010), pp. 3–6. URL: http://www.gaas.org/Digests/2010/Papers/08.4.040.pdf.

[112] MicroChem. *PMMA FAQ*. URL: http://www.microchem.com/pmma{_}faq.htm (visited on 07/02/2016).

[113] H R et al. “Improved step edges on LaA103 substrates etch masks by using amorphous carbon”. In: *Appl. Phys. Lett.* 65.9 (1994), pp. 3–5.